Quasi-Geostrophic Topographically Generated Mean Flow over the Continental Margin

ROGER M. SAMELSON AND J. S. ALLEN

College of Oceanography, Oregon State University, Corvallis, OR 97331

(Manuscript received 2 October 1986, in final form 6 April 1987)

ABSTRACT

Observations of oppositely directed, monthly mean alongshore currents and wind stress over the continental margin off the Pacific coast of North America motivate the theoretical examination of mean flow generation by topographic lee-wave drag. We formulate a barotropic model for wind-forced shelf-slope flow over variable topography. Our central objective is an analytical expression for mean flow generation in a simple case. We specify a linear cross-shelf slope with sinusoidal alongshore variations and use the approximation of Hart, which yields a system with only parametric cross-shelf dependence when the alongshore scales are short compared to the cross-shelf scales. The inviscid unforced equations have two constants of the motion and reduce to a quartic Hamiltonian system similar to that of Duffing's equation. For weak near-resonant time-periodic forcing, we use the method of averaging to obtain evolution equations for the amplitudes of small oscillations. All steady solutions of the averaged equations, which correspond to steadily oscillating small amplitude currents in the model, have mean current in the direction of the observed currents (poleward on an eastern boundary). Multiple equilibria occur. Mean current generation is most efficient for low frequencies, short wavelength topographic variations, and comparable alongshore and cross-shelf topographic slopes. The mean Lagrangian flow is along isobaths. Numerical solutions of the model equations compare well with the averaging analysis predictions. For certain parameter ranges, all steady solutions of the averaged equations are linearly unstable. In these ranges, numerical solutions of the averaged equations yield limit cycles, period doubling sequences, and chaotic behavior, suggesting that the response of slope flow to atmospheric forcing may be irregular.

1. Introduction

Observations over the continental margin off central California indicate monthly mean midshelf, middepth currents are northward all year while mean wind stresses are southward (Denbo and Allen, 1987; Strub et al., 1987). The dynamics that give rise to this mean interior flow against mean surface stress are not presently understood. Continental shelf waves have also been observed in shelf–slope flow (Enfield and Allen, 1983; Halliwell and Allen, 1984); the theory of their motion is well developed. Their phase propagates in only one direction (poleward on an eastern boundary), so they may exist as lee waves on only one side of an obstacle. The resulting wave drag will depend asymmetrically on the current (Martell and Allen, 1979) and should generate a mean flow in response to an oscillating, zero-mean wind stress. Consequently, the interaction of forced shelf flow with alongshore topographic variations is a natural candidate for a theory of the observed northward shelf currents. Here we begin the dynamical analysis of mean flow generation by topographic lee wave drag with a simple model of wind-forced flow over a bumpy continental slope. Our central objective is an analytical expression for mean flow generation in this simple case.

We specify barotropic quasi-geostrophic f-plane channel flow over a sloping bottom with sinusoidal cross-channel (cross-shelf) ridges, bottom friction, and an along-channel (alongshore) wind stress. Hart (1979) formulated a similar model to study multiple equilibria and blocking in atmospheric flow over mountains, with vortex stretching due to the beta-effect rather than the continental slope. Following Hart, we derive a simplified set of three ordinary differential equations by assuming that the alongshore velocities of the topographic wave are negligible when the alongshore wavelength of the ridges is short compared to the cross-shelf scales on which the ridge heights vary. (Charney and DeVore, 1979, obtain a similar representation by spectral truncation.) These model equations are identical to those of Hart except that the scaling is different and the forcing of interest is periodic rather than steady.

The presence of time-dependent forcing substantially complicates the problem. We restrict the analysis here to weak near-resonant forcing and use the method of averaging to obtain evolution equations for slowly varying amplitudes of small oscillations. (This effectively reduces the dimensions of phase and parameter spaces by one each.) All steady solutions of the averaged equations, which correspond to solutions of the model equations with steadily oscillating currents, have negative (poleward on an eastern boundary) mean current. Mean current generation is most efficient for low frequencies, short-wavelength alongshore topographic variations, and comparable alongshore and cross-shelf topographic slopes. The mean Lagrangian flow is along isobaths.

Mean flow generation by topographic interaction is inherently nonlinear. This nonlinearity leads to a rich variety of qualitative behavior in the averaged equations. Multiple equilibria occur. (These correspond to multiple steadily oscillating flows and thus differ from the multiple steady flows found by Hart, 1979, and Charney and DeVore, 1979.) Some steady solutions are unstable, and for parameter values near a Hopf bifurcation point no stable steady solutions exist. Numerical integrations of the averaged equations yield limit cycles, period doubling sequences, and chaotic solutions.

The averaging analysis prediction of mean current generation compares well with numerical integrations of the model equations even for forcing of nondimensional order one. The prediction of irregular response to regular forcing near resonance is briefly investigated and agreement is found for weak forcing and friction.

The model retains the essential physics of the interaction between periodically forced barotropic quasi-geostrophic shelf-slope flow and topographic wave drag, yet is simple enough to yield analytical results. It robustly predicts mean flow generation and complements recent numerical modeling work in which the real topography is better represented (Haidvogel and Brink, 1986). The appearance in the model of chaotic solutions suggests that the response of slope flow to atmospheric forcing may be irregular.

2. Equations

First, we derive the governing equations, using the approximation of Hart (1979); second, we give the scaling arguments for the oceanic continental margin case and motivate the restriction to weak near-resonant forcing.

Figure 1 displays the model geometry. We choose a right-handed Cartesian coordinate system over the continental slope with horizontal coordinates (x', y'), where x' is alongshore and positive in the direction opposite to topographic Rossby wave phase propagation, and y' is positive onshore. We confine the fluid to an alongshore channel with walls at $y = 0$ and $y = y_0'$ and a variable depth that increases offshore. (The confinement models the effect of coastal trapping and isolates the dynamics from the unspecified deep ocean fields.) We take the flow to be governed by the barotropic quasi-geostrophic potential vorticity equation (Pedlosky, 1979), which in nondimensional form is

$$\left(\frac{\partial}{\partial t}+\frac{\partial\psi}{\partial x}\frac{\partial}{\partial y}-\frac{\partial\psi}{\partial y}\frac{\partial}{\partial x}\right)(\Delta\psi+h)=-\hat{r}\Delta\psi+\frac{\partial\hat{\tau}^y}{\partial x}-\frac{\partial\hat{\tau}^x}{\partial y}. \tag{2.1}$$

Here the dimensionless streamfunction $\psi = p'/\rho U_0 fL$, coordinates $(x, y) = (x', y')/L$, time $t = t'U_0/L$, bottom topography $h = h'/\mathrm{Ro}D$, friction $\hat{r} = \delta_E/2\mathrm{Ro}D$, and vector wind stress $(\hat{\tau}^x, \hat{\tau}^y) = (\tau^{x'}, \tau^{y'})/\tau_0$. Primes denote dimensional variables; p' is pressure. The density ρ,

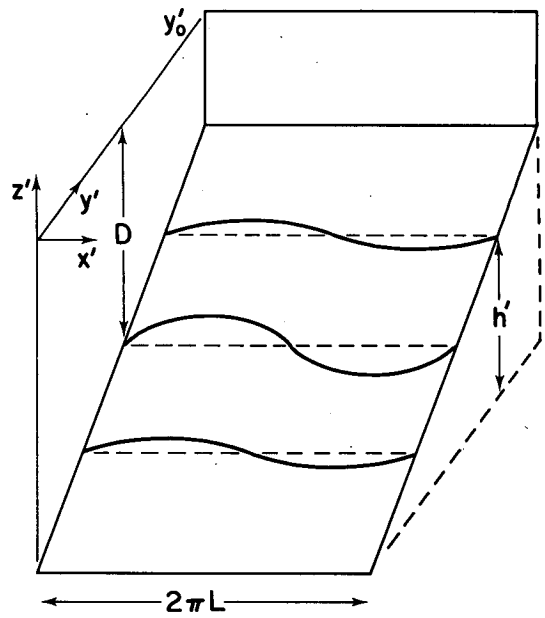

FIG. 1. Model geometry. Isobaths are schematic. We consider the case $\pi L \ll y_0'$.

Coriolis parameter f, velocity, length, and depth scales U_0, L and D, bottom Ekman layer depth δ_E, and wind stress scale $\tau_0 = \rho U_0 f$ $\mathrm{Ro}D = \rho U_0^2 D/L$ are dimensional constants, and $\mathrm{Ro} = U_0/fL$ is the Rossby number. The horizontal Laplacian $(\partial^2/\partial x^2 + \partial^2/\partial y^2)$ is denoted by Δ. We will also use subscripts to denote partial differentiation with respect to x, y, or t.

For bottom topography we take

$$h(x, y) = y + g(x, y), \tag{2.2a}$$

where g represents the topographic variations that are superimposed on the uniform cross-channel slope and has the form

$$g(x, y) = \sqrt{2}\delta(y)\cos x, \tag{2.2b}$$

$$\delta(0) = \delta(y_0) = 0, \tag{2.2c}$$

where δ is a smooth nonnegative function of y that vanishes near the channel walls. The forcing is

$$\hat{\tau}^x = \tau\cos(\omega t), \quad \hat{\tau}^y = 0. \tag{2.3}$$

The flow is periodic in x, and there is no normal flow at the channel walls:

$$\psi(x, y, t) = \psi(x + 2\pi, y, t), \tag{2.4a}$$

$$\psi_x(x, 0, t) = \psi_x(x, y_0, t) = 0. \tag{2.4b}$$

We denote by angle brackets the x-average over a topographic period and by square brackets with superscript t the t-average over a forcing period, that is,

$$\langle\Phi\rangle = \frac{1}{2\pi}\int_x^{x+2\pi}\Phi dx', \tag{2.5a}$$

$$[\Phi]^t = \frac{\omega}{2\pi}\int_{t-(\pi/\omega)}^{t+(\pi/\omega)} \Phi dt'. \tag{2.5b}$$

Averaging the depth-integrated x-momentum equation over a period in x and using (2.2), (2.3), (2.4) and (2.5), we obtain the constraint

$$\left(\frac{\partial}{\partial t}+\hat{r}\right)\langle\psi_y\rangle = -\langle\hat{\tau}^x\rangle \quad \text{at} \quad y=0, y_0. \tag{2.6}$$

Averaging (2.1) over a period in x, integrating with respect to y, and using (2.6), we obtain an equation for the x-averaged alongshore flow,

$$\left(\frac{\partial}{\partial t}+\hat{r}\right)\langle\psi_y\rangle = -\frac{\partial}{\partial y}\langle\psi_x\psi_y\rangle - \langle\psi_x g\rangle - \langle\hat{\tau}^x\rangle. \tag{2.7}$$

Integrating the second term on the right-hand side of (2.7) by parts shows

$$\langle\psi_x g\rangle = -\langle\psi g_x\rangle, \tag{2.8}$$

so the covariance between the cross-shelf velocity and the topographic height is just the wave drag, that is, the negative of the x component of the average pressure stress exerted on the topography.

Let

$$\psi(x,y,t) = -U(t)y + \phi(x,y,t), \tag{2.9}$$

where U is the basic alongshore flow and ϕ the perturbation due to the topography. Substituting (2.9) into (2.1) leads to an equation for ϕ involving U. In order to simplify the analysis of the resulting problem, we consider ridges that vary slowly across a wide channel. If y-derivatives of g are small, y-derivatives of ϕ ought to be small also. Thus, following Hart who justifies this step with a formal asymptotic expansion in the ratio of x- and y-length scales. We neglect all terms in (2.1) and (2.7) that include y-derivatives of ϕ or g, obtaining

$$\frac{dU}{dt} = -\hat{r}U + \langle\phi_x g\rangle + \langle\hat{\tau}^x\rangle, \tag{2.10a}$$

$$\phi_{xxt} = -U\phi_{xxx} - \hat{r}\phi_{xx} - \phi_x - Ug_x. \tag{2.10b}$$

Friction, x-averaged wave drag, and x-averaged wind stress determine the acceleration dU/dt of the alongshore flow in (2.10a). The vorticity ϕ_{xx} varies with time in (2.10b) in response to advection by the alongshore flow, friction, and vortex stretching (motion in the ambient potential vorticity gradient). There are two vortex stretching terms: the first is due to offshore flow over the shelf slope, the second, alongshore flow over the ridge slopes. Equations (2.10) correspond to Eqs. (5) and (4) in Hart (1979) when U, ϕ, $\hat{r}$, g and t^{-1} are divided by β and the forcing is scaled to unity.

We have required the alongshore topographic variations to vanish near the walls, so the wave drag in (2.7) and related topographic effects in (2.1) will also vanish there, and no difficulties should arise in satisfying the boundary conditions. If topographic variations are considered that do not vanish at the walls, or if discontinuities in the interior solution arise as the topographic amplitude δ varies through bifurcation points, boundary layers may be needed. We assume, as Hart did, that such boundary layers can exist. Since the subsequent analysis will show that the character of the solution depends on parameter values, slow variations in topographic amplitude may yield qualitatively different behavior at different locations, even in this simple model. Detailed consideration of this question is beyond the scope of the present paper; its objective is an understanding of the local dynamics of mean flow generation.

Fourier series expansion of ϕ in x reduces (2.10) to a set of ordinary differential equations. For the topography (2.2), this set is

$$\frac{dU}{dt} = -\hat{r}U + \delta\phi_2 + \hat{\tau}^x, \tag{2.11a}$$

$$\frac{d\phi_1}{dt} = -\hat{r}\phi_1 - (U-1)\phi_2, \tag{2.11b}$$

$$\frac{d\phi_2}{dt} = -\hat{r}\phi_2 + (U-1)\phi_1 - \delta U, \tag{2.11c}$$

where

$$\phi = \sqrt{2}(\phi_1 \cos x + \phi_2 \sin x). \tag{2.12}$$

The other Fourier coefficients of ϕ decay to zero (or remain zero if they vanish initially), and in any event do not contribute to the wave drag. The set (2.11), with $\hat{\tau}^x$ given by (2.3), is third order but nonautonomous, and has no steady solutions. It is similar to (7), (8) and (9) of Hart; the scaling is different and the forcing is periodic rather than steady. The y-dependence of ϕ is parametric, through δ.

Physical considerations suggest the use of the quasi-geostrophic approximation and give an idea of the relevant parameter ranges. We choose a barotropic model for simplicity and because the observed currents are often not strongly depth-dependent, and defer discussion of the possible effects of stratification to section 6. A typical velocity over the slope is $U_0 = 10$ cm s^{-1}. We take this to be the fundamental dynamical scale. Values appropriate to the geometry of the upper continental slope are depth $D = 250$ m, width $y_0' = 40$ km, and bottom slope $dh'/dy' = 10^{-2}$. Setting $2\pi L$ equal to the wavelength of a resonant topographic wave when $U' = U_0$ determines the length scale as

$$L = \left[U_0 D/f\left(\frac{dh'}{dy'}\right)\right]^{1/2} = 5\,\text{km}.$$

Thus at midlatitudes ($f = 10^{-4}$ s^{-1}) a typical Rossby number is Ro $= U_0/fL = 0.2$, and quasi-geostrophic theory should illuminate the physics. Since $L \ll (gD)^{1/2}/f$ (here g is gravitational acceleration) and $L \ll f/(df/dy')$, free surface deformation and variation of Coriolis parameter are neglected in (2.1). The wave-

length of the topographic variations (2.2b) is $2\pi L \approx 30$ km. Martell and Allen (1979), using digitized topographic data for the continental slope and upper shelf off Oregon from Peffley and O'Brien (1976), noted that for the lowest cross-shelf mode of topography, alongshore variations with wavelength near 30 km had an amplitude around 40 m. In dimensional form, the topography (2.2) is

$$h' = \frac{\mathrm{Ro}D}{L} y' + \sqrt{2}\delta' \cos\frac{x'}{L}, \tag{2.13}$$

where $\delta' = \mathrm{Ro}D\delta$. Using the above values, we find $\mathrm{Ro}D = 50$ m, so $\delta = \mathrm{O}(1)$ is appropriate. The alongshore length scale of topographic variation is less than the cross-shelf scale ($\frac{1}{2}\pi L \approx 8$ km < 20 km $= \frac{1}{2}y'_0$), but the ratio of the two is not asymptotically small. We persist with the limit of anisotropic topography in the model because of the accompanying simplification of the analysis. Recent numerical results (Haidvogel and Brink, 1986) suggest that short-wavelength topography is most effective in generating mean flow, so the limit of short wavelength is of natural interest.

For a dimensional alongshore wind stress of 1 dyn cm^{-2} and a bottom Ekman layer depth of $\delta_E = 10$ m (corresponding to a dimensional frictional time scale $T_F = 2D/(\delta_E f) \approx 6$ days), the nondimensional wind stress and friction parameters are $\hat{\tau}^x = 0.2$, $\hat{r} = 0.1$. Since these values are small, and since the resulting problem is relatively tractable, we restrict the analysis here to weak forcing and weak friction. We have chosen the topography to give resonance when the alongshore velocity $U = 1$, so the small-amplitude analysis in effect treats the interaction of forced flow with topography that has wavelength longer than the resonant scale. Numerical solutions in section 4 indicate that the mean current prediction from this analysis maintains substantial accuracy for $\hat{\tau}^x$, $\hat{r}$, $U = \mathrm{O}(1)$.

The time scale L/U_0 is about 0.6 days, so the forcing period $2\pi L/\omega U_0$ is about $4/\omega$ days. Consequently, $\omega = \mathrm{O}(1)$ is appropriate for wind stress forcing by synoptic-scale weather systems. Subsequent analysis will show that the system (2.11) has oscillatory solutions when friction and forcing vanish. At small amplitude, the frequency of linear oscillations is also O(1) if $\delta = \mathrm{O}(1)$, so that natural and forcing frequencies are of the same order in this limit. Motivated by this and the belief that a dynamical system's response to forcing is often both most interesting and most important near resonance, we examine the behavior of (2.11) for near-resonant forcing.

3. Analysis

a. *Inviscid unforced oscillations*

When friction and forcing vanish in (2.1), multiplication by ψ and $(\Delta\psi + h)$ and integration over the channel area yield conservation statements for the area integrals of kinetic energy $\frac{1}{2}(\psi_x^2 + \psi_y^2)$ and potential enstrophy $\frac{1}{2}(\Delta\psi + h)^2$, respectively (Pedlosky, 1979). When friction and forcing vanish in (2.10), similar statements exist for x-averaged quantities:

$$\frac{d}{dt}\left(\frac{1}{2}U^2 + \frac{1}{2}\langle\phi_x^2\rangle\right) = 0, \tag{3.1a}$$

$$\frac{d}{dt}\left(\frac{1}{2}\langle\phi_{xx}^2\rangle + \langle\phi_{xx}g\rangle + U\right) = 0. \tag{3.1b}$$

The first, (3.1a), expresses conservation of x-averaged kinetic energy. The second, (3.1b), is the x-average of the equation for potential enstrophy conservation. The third term in the second equation, dU/dt in (3.1b), is equal to the x-average of the cross-shelf advective derivative of potential enstrophy, by (2.10a). The quantity conserved in (3.1b) is equal to the x-averaged potential enstrophy only if $U = 0$.

For (2.11), the corresponding conservation statements are

$$\frac{dE}{dt} = 0, \tag{3.2a}$$

where

$$E = \frac{1}{2}(U^2 + \phi_1^2 + \phi_2^2), \tag{3.2b}$$

$$\frac{dM}{dt} = 0, \tag{3.2c}$$

where

$$M = \frac{1}{2}(\phi_1^2 + \phi_2^2) - \delta\phi_1 + U. \tag{3.2d}$$

Consequently, when friction and forcing vanish, the system (2.11) has only one degree of freedom. In fact it has periodic solutions and may be solved in terms of elliptic functions (Charney and De Vore, 1979).

For convenience, we introduce new variables to replace ϕ_1 and ϕ_2, rewriting (2.11) as

$$\frac{dU}{dt} = -\hat{r}U + F + \tau\cos\omega t, \tag{3.3a}$$

$$\frac{dF}{dt} = -\hat{r}F + (U-1)G - \omega_0^2 U + \frac{3}{2}U^2 - \frac{1}{2}U^3, \tag{3.3b}$$

$$\frac{dG}{dt} = -\hat{r}G - \frac{1}{2}\hat{r}U^2 + (U-1)\tau\cos\omega t, \tag{3.3c}$$

where

$$F = \delta\phi_2, \tag{3.4a}$$

$$G = E - M, \tag{3.4b}$$

$$\omega_0^2 = 1 + \delta^2. \tag{3.5}$$

It is evident from (3.3) that the inviscid unforced system is Hamiltonian with Hamiltonian function

$$H(U,F) = \frac{1}{2}F^2 + GU + \frac{1}{2}(\omega_0^2 - G)U^2 - \frac{1}{2}U^3 + \frac{1}{8}U^4 = \delta^2 E - \frac{1}{2}G^2. \tag{3.6}$$

The conserved quantity G appears only as a parameter; the square of the linear frequency is $\omega_0^2 - G$. If $G = 0$ and δ is O(1), the linear frequency is O(1). Since by (3.4b) and (3.2b), G is a continuous function on an energy sphere $E = E_0$, it is bounded for a given value E_0. Crudely, $|G| \leqslant \sqrt{E_0}[\sqrt{E_0} + \sqrt{2}(1 + \delta)]$. The Hamiltonian (3.6) is quartic like that of Duffing's equation (Duffing, 1918; or, e.g., Nayfeh and Mook, 1979) but not symmetric.

b. Averaged equations

Equations (3.3) are nonlinear, have no steady solutions, and depend on three parameters, so direct study of them is difficult. Analytical progress can be made at small amplitude, where the nonlinear effects are small. We use the method of averaging to approximate asymptotic solutions for weak near-resonant forcing.

Anticipating the scaling that will allow forcing, friction, and nonlinearity to enter at the same order, we let

$$\epsilon = \tau^{1/3}, \tag{3.7a}$$

$$r = \hat{r}/\epsilon^2, \tag{3.7b}$$

$$\sigma = (\omega^2 - \omega_0^2)/2\epsilon^2\omega, \tag{3.7c}$$

and consider $0 < \epsilon \ll 1$, $r > 0$ and $r, \sigma = O(1)$.

With this scaling, all solutions eventually have $U, F = O(\epsilon)$, $G = O(\epsilon^2)$, as shown in appendix A. To investigate the details of the asymptotic behavior, we use the method of averaging. We give the results of the averaging procedure here; the details are in appendix A.

With the variables (U, F, G) expressed as

$$U = \epsilon(Ze^{i\omega t} + \bar{Z}e^{-i\omega t}) + \epsilon^2(u_1 e^{i\omega t} + \bar{u}_1 e^{-i\omega t}), \tag{3.8a}$$

$$F = \epsilon[i\omega(Ze^{i\omega t} - \bar{Z}e^{-i\omega t})] + \epsilon^2[i\omega(u_1 e^{i\omega t} - \bar{u}_1 e^{-i\omega t})], \tag{3.8b}$$

$$G = \epsilon^2 C, \tag{3.8c}$$

where Z is complex, C is real, overbar denotes complex conjugate, and

$$u_1 = -\frac{3Z^2}{4\omega^2}e^{i\omega t} + \frac{1}{2\omega^2}(3Z\bar{Z} - C)e^{-i\omega t} + \frac{\bar{Z}^2}{4\omega^2}e^{-3i\omega t}, \tag{3.9}$$

the averaged equations are

$$\frac{dZ}{dt} = \epsilon^2\left[-rZ - i\sigma Z + \frac{1}{2}k + ib_1 ZC + ib_2 Z^2\bar{Z}\right], \tag{3.10a}$$

$$\frac{dC}{dt} = \epsilon^2\left[-rC - rZ\bar{Z} + \frac{1}{2}(Z + \bar{Z})\right]. \tag{3.10b}$$

Here

$$k = \frac{\delta^2}{2\omega_0^2}, \tag{3.11a}$$

$$b_1 = -\frac{1}{2\omega_0}\left(1 - \frac{3}{\omega_0^2}\right), \tag{3.11b}$$

$$b_2 = \frac{3}{4\omega_0}\left(1 - \frac{5}{\omega_0^2}\right), \tag{3.11c}$$

and (3.7c) has been used to replace ω by ω_0 with no loss of accuracy. In appendix A, we discuss the error incurred in using solutions of (3.10) in (3.8) to approximate solutions of (3.3).

Averaging over the forcing period and neglecting the error terms, we obtain, using (2.5b),

$$(\epsilon^2 \lim_{\epsilon \to 0} \epsilon^{-2})[U]^t = \epsilon^2 U_m = \epsilon^2\left(\frac{3\bar{Z}Z - C}{\omega_0^2}\right), \tag{3.12}$$

which defines the (time) mean current U_m. This local time mean may vary slowly according to (3.10).

For numerical solution, it is convenient to write the averaged equations in terms of the real and imaginary parts of Z. Letting

$$Z = Z_R + iZ_I, \tag{3.13}$$

(3.10) becomes:

$$\frac{dZ_R}{dT_2} = -rZ_R + \sigma Z_I - b_1 Z_I C - b_2(Z_R^2 + Z_I^2)Z_I + \frac{1}{2}k, \tag{3.14a}$$

$$\frac{dZ_I}{dT_2} = -rZ_I - \sigma Z_R + b_1 Z_R C + b_2(Z_R^2 + Z_I^2)Z_R, \tag{3.14b}$$

$$\frac{dC}{dT_2} = -rC - r(Z_R^2 + Z_I^2) + Z_R, \tag{3.14c}$$

where $T_2 = \epsilon^2 t$.

Applying the method of multiple time scales (Kevorkian and Cole, 1981) to (3.3) gives equations equivalent to (3.10).

c. Steady solutions and mean flow generation

The steady solutions of (3.10) correspond to periodic solutions of the original set (2.11) with amplitude constant to first order, as can be seen from (3.8).

For convenience, we first transform Z to a polar form,

$$Z(t) = \frac{1}{2}a(t)e^{i\gamma(t)}, \tag{3.15}$$

where a and γ are real. [By (3.8), $U = \epsilon a \cos(\omega t + \gamma) + O(\epsilon^2)$.] Then the steady solutions (a_0, γ_0, C_0) of (3.10) are found by setting the time derivatives equal to zero and solving the resulting algebraic problem. The squared steady amplitude satisfies the cubic equation

$$P(a_0^2) = 0, \tag{3.16a}$$

where

$$P(a^2) = [r^2 + (\sigma - \alpha a^2)^2]a^2 - k^2, \tag{3.16b}$$

and γ_0 and C_0 are determined from

$$\gamma_0 = \arctan\left[-\frac{(\sigma - \alpha a_0^2)}{r}\right], \tag{3.17a}$$

$$C_0 = \left(\frac{3}{4} + \frac{1}{\delta^2}\right) a_0^2, \tag{3.17b}$$

where

$$\alpha = \frac{1}{16\delta^2\omega_0^3}(4 - 3\delta^2)(4 + \delta^2). \tag{3.18}$$

It follows from (3.15) and (3.17b) and the expression for the mean current U_m (3.12) that

$$U_{m_0} \equiv U_m(a_0^2) = -\frac{a_0^2}{\delta^2\omega_0^2}, \tag{3.19}$$

so all steady solutions have negative mean current. [Solutions with $a_0^2 = 0$ are only possible if $\delta = 0$, as evident from (3.16) and (3.15a).] This is our central result on mean flow generation.

Since for fixed δ, by (3.19), the magnitude of the mean current U_{m_0} increases with the oscillation amplitude a_0, the largest solution of (3.16) yields the maximum (negative) mean current for given δ. The largest solution of (3.16) as σ varies for given δ and r is $a_0^2 = k^2/r^2$ (section 3d). After the use of (3.7) and (3.11a), the corresponding maximum mean current is

$$[U]'_{0,\max} = -\frac{\delta^2\tau^2}{4(1 + \delta^2)^3\hat{r}^2}. \tag{3.20}$$

Its magnitude increases as the square of the ratio of forcing τ to friction $\hat{r}$ and has a maximum for given τ and $\hat{r}$ at topographic amplitude $\delta = 1/\sqrt{2}$. We discuss the dimensional form of (3.20) in section 5.

d. *Multiple equilibria*

Equation (3.16) is identical in form to an equation that results from a similar perturbation analysis of Duffing's equation (Nayfeh and Mook, 1979, section 4.1). Solutions depend on the three parameters r, σ and δ, since k depends directly on δ by (3.5) and (3.11a). The graph of amplitude versus the frequency parameter σ for fixed r and δ (the frequency-response curve) can be constructed easily by solving (3.16) as a quadratic equation for σ, which gives

$$\sigma = \alpha a_0^2 \pm \left(\frac{k^2}{a_0^2} - r^2\right)^{1/2} \tag{3.21a}$$

and noting that real solutions exist for

$$0 < a_0^2 \leq \frac{k^2}{r^2}. \tag{3.21b}$$

In the following, "right branch" means the plus sign in (3.21a) and "left branch" means the minus sign. A typical response curve has a peak near resonance ($\sigma = 0$) that is smoothed by friction and bent by the nonlinearity. Figure 3, discussed below, shows examples of such curves.

Substituting (3.21a) in (3.17a) and solving for the squared amplitude shows

$$a_0^2 = \frac{k^2}{r^2}\cos^2\gamma_0, \tag{3.22}$$

so the amplitude of the basic alongshore flow decreases as the magnitude of the phase difference between it and the forcing increases.

For certain parameter values, (3.16) has multiple solutions. As δ and r vary through the point where bifurcation to multiple equilibria on the response curve occurs, the tangent to the response curve passes through the vertical and three distinct real solutions of (3.16) emerge from one. The bifurcation set is the set of solutions to

$$P(a_c^2) = P'(a_c^2) = P''(a_c^2) = 0, \tag{3.23}$$

where prime denotes differentiation with respect to a^2. Solving (3.23), we obtain

$$\frac{k^2|\alpha|}{r^3} = \frac{8}{3\sqrt{3}}, \tag{3.24a}$$

$$(\sigma_c, a_c^2) = \left(\frac{\sqrt{3}r\alpha}{|\alpha|}, \frac{2r}{\sqrt{3}|\alpha|}\right), \tag{3.24b}$$

where the vertical tangent occurs at (σ_c, a_c^2). Multiple equilibria occur if

$$\frac{k^2|\alpha|}{r^3} > \frac{8}{3\sqrt{3}}. \tag{3.25}$$

Thus, except at $\delta = 2/\sqrt{3}$, where $\alpha = 0$, multiple equilibria always occur for sufficiently small friction.

e. *Stability of steady solutions*

A linear stability analysis demonstrates that where there are three distinct steady solutions of (3.10), one of them is always unstable, and that for certain parameter ranges all steady solutions of (3.10) are unstable. We summarize the results of the stability analysis here and give the details in appendix C. For small r, we obtain analytical results. For general r, we use analysis and numerical methods.

Figure 2 is a bifurcation diagram for the frequency-response curves. For each δ and r there is a response curve giving the amplitude a_0^2 as a function of the frequency parameter σ. The character of the response curve depends on the region of Fig. 2 in which it lies. We give a detailed explanation of the bifurcation diagram in appendix C. The qualitative nature of the response curves in each region in Fig. 2 may be readily understood from Fig. 3, which displays a typical response curve from each region. The solid line in Fig. 2 is (3.24a); below it, multiple equilibria exist for certain σ-intervals. Thus, multiple equilibria exist in regions

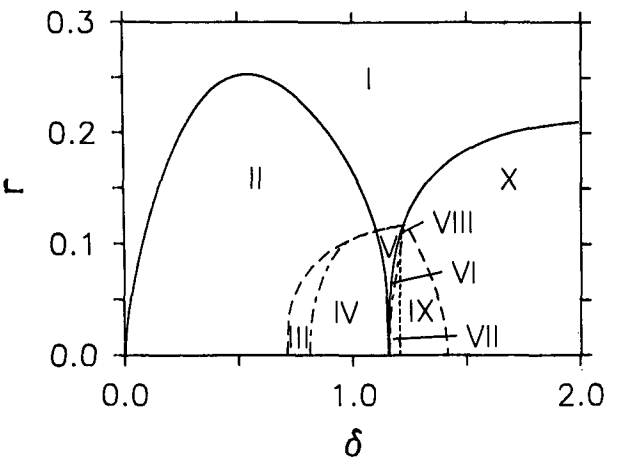

FIG. 2. Frequency-response curve bifurcation diagram. Numerals label regions as explained in text. Solid line: bifurcation to multiple equilibria; dashed lines: bifurcations to instability.

II–IV and VI–X, but not in regions I and V. All steady solutions are unstable for certain σ-intervals in regions IV, V, VI and VIII.

Where three steady solutions exist, the solution with intermediate amplitude is always unstable. At the endpoints of a σ-interval for which multiple equilibria occur, two solutions merge in a single solution that may be either unstable or neutrally stable. We call these bifurcation points (where two solutions merge and stability changes) $p_1 = (\sigma_1, a_{01}^2)$ and $p_2 = (\sigma_2, a_{02}^2)$, where $a_{02}^2 > a_{01}^2$. In addition, there is an interval of instability which is not simply related to the shape of the response curve. We call its endpoints $p_3 = (\sigma_3, a_{03}^2)$ and $p_4 = (\sigma_4, a_{04}^2)$, where $a_{04}^2 > a_{03}^2$. (All four points appear in Fig. 3c, for example. A solid curve indicates stability, a dashed curve instability, and the bifurcation points are labeled.)

In spite of the complexity of Fig. 2, the dependence of the σ-coordinate of the bifurcation points on r and δ is relatively simple. Figure 4 shows σ_i, $i = 1, \cdots, 4$, versus δ for $r = 0.05$. The points σ_1 and σ_2 describe two wedgelike regions that are separated by a gap between their tips (the gap lies in region V in Fig. 2). Multiple equilibria exist in the interiors of the wedges. Likewise, the points σ_3 and σ_4 describe a triangle with two rounded corners and a wedge attached to the sharp (lower right) corner. Inside the triangle, the left branch solution is unstable. In the small areas between the dashed wedge (σ_3 and σ_4) and the right-hand solid wedge (σ_1 and σ_2), there are multiple unstable steady solutions. Other such graphs for $r \leqslant 0.09$ are qualitatively similar. Figure 5 shows the same points versus r for $\delta = 1$. The pairs (σ_1, σ_2) and (σ_3, σ_4) each describe wedgelike regions that open rapidly as r decreases and close as r increases. Inside these regions, there are multiple equilibria and instability on the left branch, respectively. Other such graphs for $0.97 \leqslant \delta \leqslant 1.07$ are qualitatively similar.

4. Numerical integrations

a. Limit cycles, period doubling, chaotic behavior

For certain σ-intervals in regions IV, V, VI, and VIII of Fig. 2, all steady solutions are unstable and the dominant response will be unsteady. In these intervals, numerical integrations of (3.14) indicate that asymptotic behavior of solutions depends delicately on parameter values and can be complicated. Limit cycles and sequences of bifurcations to subharmonics are observed. Some solutions appear to be "chaotic" or aperiodic. Similar results have been obtained in a recent analysis of weakly nonlinear resonantly forced surface waves (Miles, 1984a; see also Miles, 1984b,c).

Region IV is the largest of the four regions of Fig. 2 for which σ-intervals with no stable steady solutions exist. In region IV, the single steady solution is unstable for $\sigma_3 < \sigma < \sigma_1$. For $\sigma < \sigma_3$, it is stable; for $\sigma_1 < \sigma < \sigma_4$, there is a stable small-amplitude steady solution in addition to the two unstable ones at larger amplitude. For the case $\delta = 1$, (3.14) were integrated numerically for various values of r and σ, with $0.01 \leqslant r \leqslant 0.08$, $-0.1 \leqslant \sigma \leqslant 0.5$. (Fig. 3d is the response curve for $\delta = 1$, $r = 0.05$, and Fig. 5 shows the points of bifurcation to instability for $\delta = 1$; they are qualitatively similar to the corresponding graphs elsewhere in region IV.)

Figure 6 and Table 1 summarize the results of these integrations. At (r, σ) in Fig. 6 (integer multiples of 0.01 and 0.05, respectively), "0" indicates an attracting steady solution for these parameter values, "T" a limit cycle, "nT" a period nT (subharmonic) limit cycle, and "Ch" a chaotic solution. We call a solution "chaotic" here if it is associated with a subharmonic bifurcation sequence and does not settle down to recognizable periodic behavior by time $T_2 = 10\,000$, roughly several hundred typical limit-cycle periods. (For $\epsilon^3 = \tau = 0.2$ and the scaling of section 2, the dimensional time is roughly $2T_2$ days.)

Table 1 includes results for additional σ at $r = 0.02$, with similar notation. For those σ (at $r = 0.02$) for which all numerical solutions appeared chaotic, the positive Lyapunov exponent (λ_1) is also given in Table 1. The Lyapunov exponents, which were calculated by the method of Wolf et al. (1985), measure the average exponential rate of divergence of nearby trajectories along the attractor in phase space. A positive exponent indicates divergence of trajectories and is further numerical evidence that the solution is aperiodic (not a stable long-period limit cycle). The uncertainty in the values of λ_1, estimated from the convergence of the calculations, is a few percent.

The analysis of appendix C shows that the bifurcation at p_3 is a Hopf bifurcation for small r. Since, for $\sigma < \sigma_3$, only a stable steady solution is observed numerically, and for $\sigma > \sigma_3$, only a stable periodic solution near the (unstable) steady solution, the numerical results suggest that the bifurcation is supercritical (a stable limit cycle emerges from a stable steady solution). It

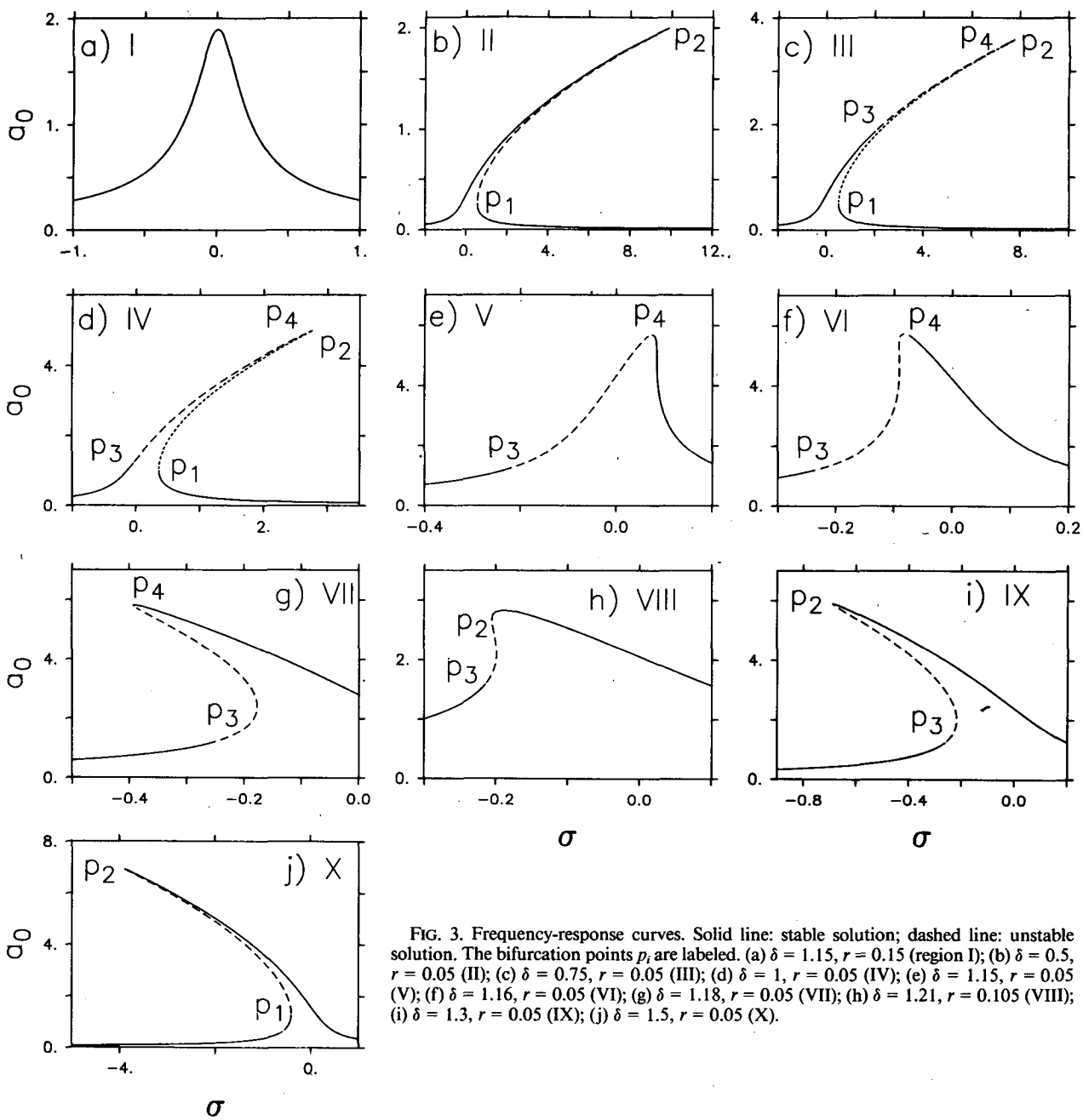

FIG. 3. Frequency-response curves. Solid line: stable solution; dashed line: unstable solution. The bifurcation points p_i are labeled. (a) $\delta = 1.15$, $r = 0.15$ (region I); (b) $\delta = 0.5$, $r = 0.05$ (II); (c) $\delta = 0.75$, $r = 0.05$ (III); (d) $\delta = 1$, $r = 0.05$ (IV); (e) $\delta = 1.15$, $r = 0.05$ (V); (f) $\delta = 1.16$, $r = 0.05$ (VI); (g) $\delta = 1.18$, $r = 0.05$ (VII); (h) $\delta = 1.21$, $r = 0.105$ (VIII); (i) $\delta = 1.3$, $r = 0.05$ (IX); (j) $\delta = 1.5$, $r = 0.05$ (X).

appears to persist for finite r. Continuity as p_3 approaches p_4 and numerical determinations of eigenvalues suggest that p_4 is also a Hopf bifurcation point.

Period-doubling sequences occur at constant r as σ is increased over most of the interval. Such sequences of bifurcations to subharmonics are often associated with transitions to chaotic behavior (Feigenbaum, 1983). (Note also the appearance, typical of chaotic regimes, of an odd period subharmonic at $r = 0.04$, $\sigma = 0.2$, indicated in Fig. 6.) We examine in more detail the sequence for increasing σ at $r = 0.02$. Figure 7 displays phase space trajectories [projected onto the (C, Z_R) plane] and the corresponding solutions C versus T_2. The limit cycle at $\sigma = 0$ is shown in Fig. 7a. The "×" marks the projection of the unstable steady solution. Figure 7c displays the limit cycle at $\sigma = 0.2$. The amplitude has increased, and the period has doubled. Figure 7e displays the limit cycle at $\sigma = 0.215$. Again the period has doubled, to four times the original value, and the amplitude has increased. The period of the limit cycle at $\sigma = 0$ is about 33, so (using the above scaling) roughly two months in dimensional units.

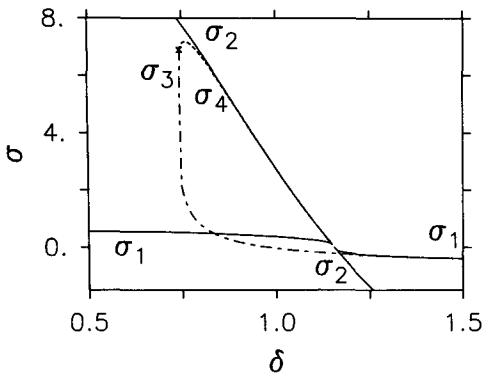

FIG. 4. σ-coordinates of bifurcation points versus δ at $r = 0.05$. "×" marks $\sigma_3 = \sigma_4$.

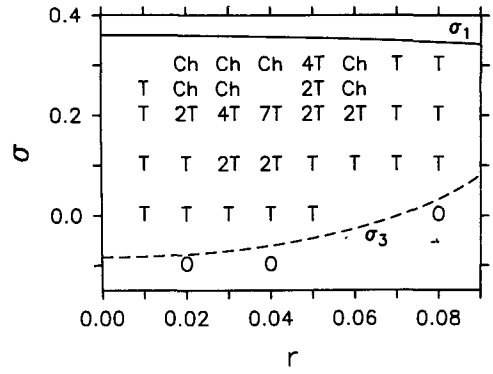

FIG. 6. Summary of numerical solutions at $\delta = 1$ as a function of σ and r: 0, steady solution; T, periodic solution; nT, period nT subharmonic; Ch, chaotic solution. Solid line: σ_1; dashed line: σ_3.

Figure 8 displays results at $\sigma = 0.225$ and $\sigma = 0.23$. At these parameter values, the system apears to have aperiodic solutions. The initial conditions for these calculations have been changed to eliminate transient behavior that is similar to that in Figs. 7b, d, f but persists much longer, and the scales on the plots have been altered. The trajectories are confined to regions near the periodic solutions in Fig. 7, but do not settle down to periodic motion.

Figure 9 displays part of a trajectory at $\sigma = 0.25$. This solution also appears aperiodic. Now however the variable C attains much larger values (greater than 30). Sudden spikes of large negative mean current U_m (3.12) appear intermittently, followed by a decay to smaller amplitude oscillations resembling those for $\sigma = 0.23$. The sudden spikes in mean current are due primarily to sudden increases in the variable C, as is evident from Fig. 9. For unsteady solutions, errors of the same order in ϵ as the mean current may accumulate on the T_2 time scale (see appendix A). [Unsteady U, F and G are rigorously approximated by the first terms on the right-hand side of (3.8) on the T_2 time scale for small ϵ, but the mean current comes from the second term on the right-hand side of (3.8a).] For corresponding parameter ranges, however, numerical solutions of the original equations (2.11) have mean currents with a similar irregular time-dependence.

To further analyze the solutions of Fig. 8, we consider their successive intersections with the half-plane $Z_R = 0$, $Z_I > 0$, $-\infty < C < \infty$. [This is similar to a Poincare map (Hirsch and Smale, 1974, section 13.3), except that a periodic solution passing through the half-plane need not exist.] Figure 10a is a plot of 304 such intersections for the solution at $\sigma = 0.23$. They appear to lie nearly on a single curve, so that the attractor crudely resembles a two-dimensional surface at its intersection with this half-plane (and in fact at all other transverse half-planes examined, though the corresponding curves are not always so simple). To characterize the motion on the attractor, we plot the Z_I-component of each intersection against the Z_I-component of the previous intersection (because the curve in Fig. 10a is nearly a line, using the C-component would give a similar result). The result is shown in Fig. 10b. Its simplicity is striking. Similar maps constructed on other half-planes were more complicated.

Also plotted in Fig. 10b is a line representing the map

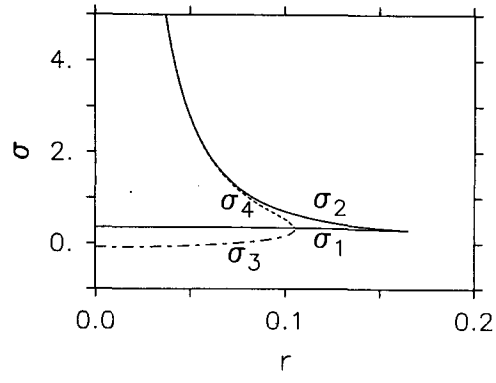

FIG. 5. σ-coordinates of bifurcation points versus r at $\delta = 1$.

TABLE 1. Summary of numerical integrations at $\delta = 1$, $r = 0.02$. The positive Lyapunov exponent λ_1 is given where a single, chaotic attractor was observed.

σ	Asymptotic behavior
0.	Steady
0.1, 0.15, 0.16, 0.165	Limit cycle, period T
0.17, 0.18, 0.19, 0.2, 0.205	Limit cycle, period $2T$
0.21, 0.215	Limit cycle, period $4T$
0.22	Limit cycle, period $8T$
0.225	Chaotic, $\lambda_1 = 0.0066$
0.23	Chaotic, $\lambda_1 = 0.0097$
0.25	Chaotic, $\lambda_1 = 0.0216$
0.3	Chaotic, $\lambda_1 = 0.0209$
0.35	Chaotic, $\lambda_1 = 0.0211$
0.5	Steady or chaotic

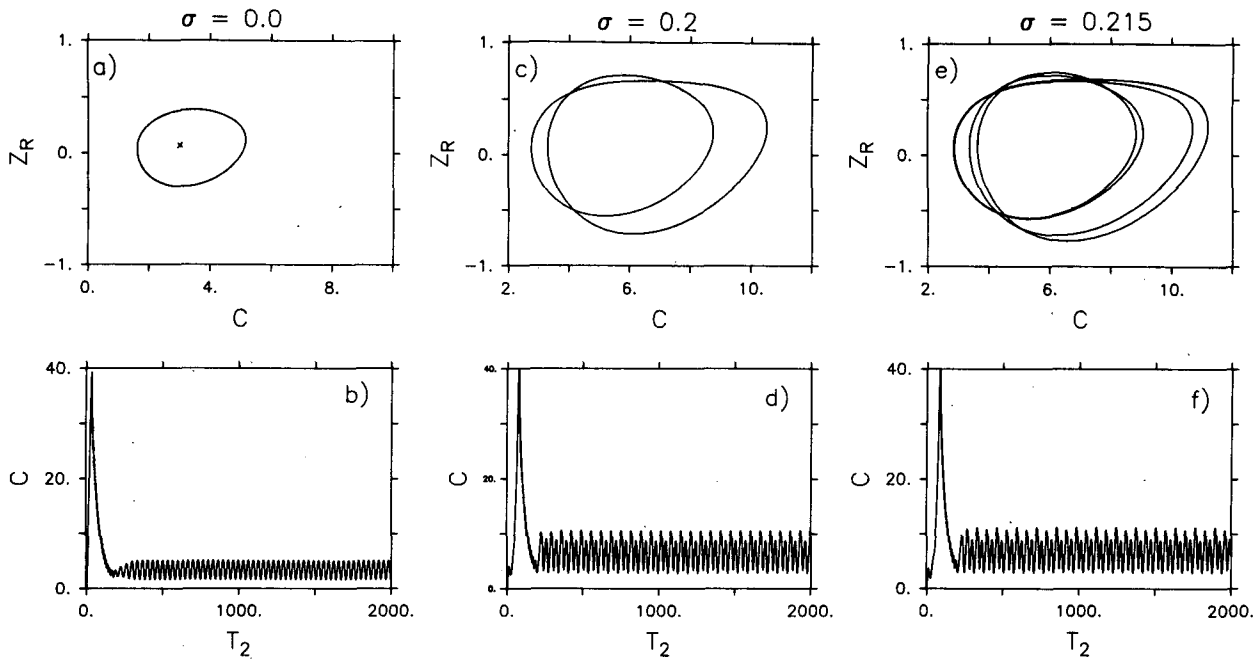

FIG. 7. Numerical solutions at $\delta = 1$, $r = 0.02$. (a) limit cycle and unstable steady solution (X) at $\sigma = 0$, projected onto (C, Z_R) plane; (b) C versus T_2 at $\sigma = 0$; (c) limit cycle, $\sigma = 0.2$; (d) C versus T_2, $\sigma = 0.2$; (e) limit cycle, $\sigma = 0.215$; (f) C versus T_2, $\sigma = 0.215$.

$$y = g^{-1}\{f[g(x)]\}, \tag{4.1}$$

where

$$f(x) = \mu x(1-x), \tag{4.2}$$

$$g(x) = [(x-x_0)/0.33]^{1/3.2}, \tag{4.3}$$

with the parameters $\mu = 3.7$, $x_0 = 1.18$. The first of these, (4.2), is the logistic map; the second, (4.3), a continuous map with a continuous inverse from the interval $(x_0, x_0 + 0.33)$ to the interval (0, 1). [Our search for an appropriate transformation of (4.2) was stimulated by Shaw (1981), and the values of the constants in (4.2) and (4.3) were determined by trial and error.] The dynamics of the map (4.2) are relatively well understood (Collet and Eckmann, 1980; Preston, 1983). The trajectories of points under iteration of (4.1) are just those of (4.2) with the coordinates changed. As the parameter μ is increased, the trajectories of (4.2) undergo period-doubling bifurcations until an accumulation point is reached near $\mu = 3.57$. For $3.57 \leqslant \mu \leqslant 4$, the motion has been called chaotic. In this case, "chaotic" means that for given μ, an infinite number of unstable periodic cycles with different periods exists, as well as an uncountably infinite number of points through which the trajectories are aperiodic. A single stable periodic cycle, possibly of very long period, may exist simultaneously, and will attract most trajectories if it does exist (Collet and Eckmann, 1980). The long transients associated with the many periodic and aperiodic points and the length of the stable periodic cycle may make the motion appear irregular even in this case (May, 1976).

The correspondence of the curve in Fig. 10b with the plot of successive intersection points is not exact; one can see that some points lie appreciably far from it and that a second curve appears to branch off the first near $(Z_I)_n = 1.35$. Also, the map is noninvertible, whereas solutions to differential equations are invertible by uniqueness. The close agreement does suggest that the asymptotic motion can be usefully described [after a simple change of coordinates close to (4.3)] by the one-dimensional map (4.1), that is, the map gives good predictions over substantial time intervals. Since points can have either periodic or aperiodic behavior under iteration of (4.1) with μ close to 3.7, we cannot infer from properties of the map that the solution of (3.14) is in fact aperiodic.

Figure 11a displays half-plane intersection points and Fig. 11b their successive Z_I-components for the solution at $\sigma = 0.225$. The curve in Fig. 11b is again (4.1), with $\mu = 3.64$, $x_0 = 1.175$, and the other constants in (4.3) unchanged. As before, the asymptotic motion is well described by the map.

These results suggest that (4.1) might describe the asymptotic motion of solutions at $\delta = 1$, $r = 0.02$ for a range of σ, if the proper dependence of μ and x_0 on σ were known. Using the two pairs of points determined above, $(\sigma, \mu) = (0.23, 3.7), (0.225, 3.64)$ and $(\sigma, x_0) = (0.23, 1.18), (0.225, 1.175)$, we approximate this dependence as linear plus a constant:

$$\mu = 3.64 + 12(\sigma - 0.225), \tag{4.4}$$

$$x_0 = 1.175 + (\sigma - 0.225). \tag{4.5}$$

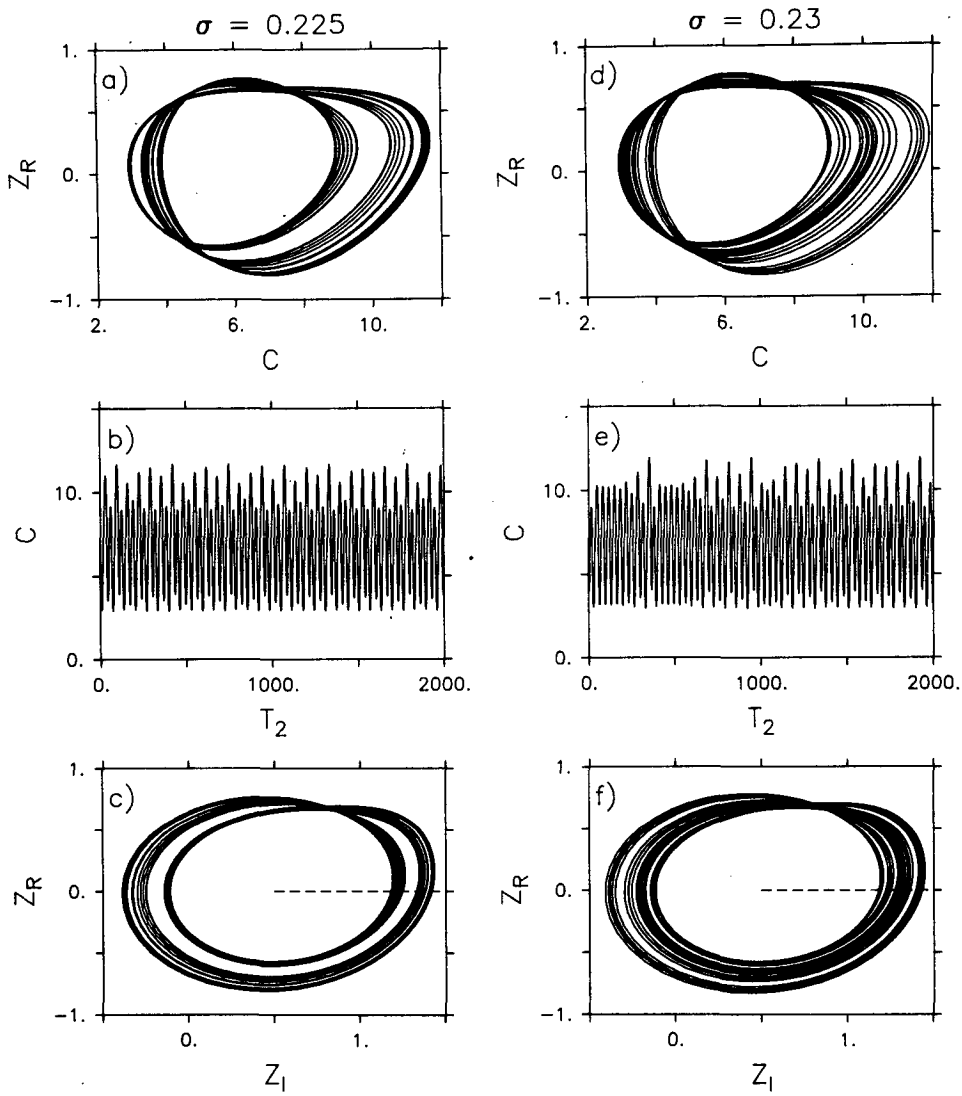

FIG. 8. Numerical solutions at $\delta = 1$, $r = 0.02$. (a) Z_R versus C at $\sigma = 0.225$; (b) C versus T_2 at $\sigma = 0.225$; (c) Z_R versus Z_I at $\sigma = 0.225$ (dashed line: projection of half-plane $Z_R = 0$, $Z_I > 0.5$, $-\infty < C < \infty$); (d), (e), (f) as (a), (b), (c) except $\sigma = 0.23$.

For $1 < \mu \leqslant 3.57$, the map (4.1) has attracting periodic orbits. For $0 \leqslant \sigma \leqslant 0.22$, numerical solutions of (3.14) approached limit cycles. We compare the Z_I-components of the points where the limit cycles intersect the half-plane with the periodic points of (4.1), using (4.4) and (4.5) to determine μ and x_0 at each σ. Figure 12 shows the result. The solid line represents the periodic points of the map and a + marks the Z_I-component of each limit cycle intersection point. The detailed agreement is remarkable. It demonstrates that a wide range of the complicated behavior observed in the numerical solutions can be described well by a simple one-parameter family of one-dimensional maps. Feigenbaum (1983) has outlined a related and more general procedure to approximate successively period-doubled limit cycles using the universal properties of period-doubling in one-dimensional maps, passing from small period toward large period cycles.

For $\sigma > 0.23$, the solutions, and thus the plots of half-plane intersection points, become more complicated. Figure 13a displays the half-plane intersections and Fig. 13b their successive Z_I-components for the solution at $\sigma = 0.25$. Whereas at $\sigma = 0.225$ and $\sigma = 0.23$ the intersections appeared to lie near a single curve, at $\sigma = 0.25$ the intersections appear to lie near a number of such curves. The plots of successive intersections show the remnant of the simple structure at $\sigma = 0.225$ and $\sigma = 0.23$. Along with it is a more complicated structure that appears to have arisen from the branch that already has begun to diverge from the curve (4.1) in Fig. 10b near $(Z_I)_n = 1.35$.

At $\sigma = 0.5$, the solution still appears chaotic (Table

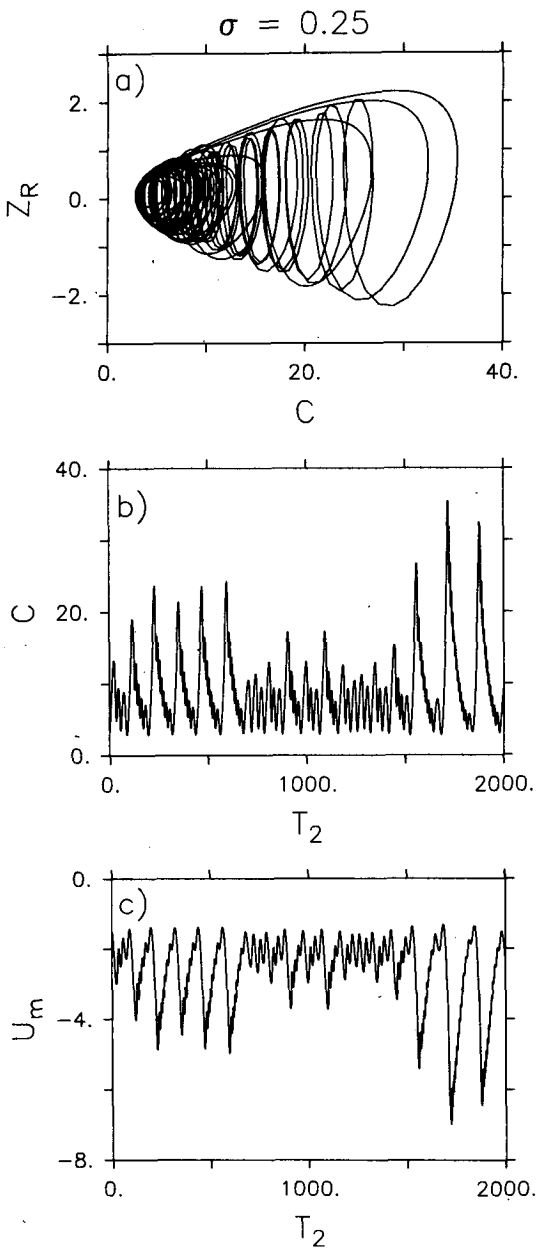

FIG. 9. Numerical solution at $\delta = 1$, $r = 0.02$, $\sigma = 0.25$. (a) Z_R vs C; (b) C vs T_2; (c) U_m vs T_2.

1). Note from Fig. 6 that $\sigma_1 < 0.5$, so at $\sigma = 0.5$ a stable small amplitude steady solution coexists with the chaotic attractor. When σ was increased past 1.0, numerical solutions tended asymptotically to the stable steady solution even when initial conditions were chosen from chaotic solutions at slightly smaller σ.

Region V is the second largest of the four regions of Fig. 2 for which σ-intervals with no stable steady solutions exist. There are no multiple equilibria in region V. (A typical response curve is Fig. 3e.) We have computed numerical solutions in this region at $\delta = 1.1547$, $r = 0.02$, and various σ, with unusual results. A small-amplitude limit cycle occurs near the Hopf bifurcation at p_3. As at $\delta = 1$, this limit cycle undergoes period doubling and becomes chaotic as σ is increased. However, there is in addition a large-amplitude limit cycle, which passes through the small-amplitude limit cycle in phase space. The large-amplitude limit cycle persists as σ is varied during and after the period-doubling transition to chaos of the small one. Thus the regularity or irregularity of the response may depend on initial conditions as well as parameter values. Figure 14a shows the large-amplitude limit cycle at $\sigma = -0.225$ projected onto the C-Z_I plane. Note its resemblance to the large-amplitude chaotic solutions of Fig. 9. Figure 14b shows the (Z_R, Z_I) projection of a portion of the large-amplitude limit cycle passing through the small-amplitude chaotic attractor at $\sigma = -0.225$.

b. Numerical solution of forced Hart equations

We briefly compare the results of the averaging analysis with numerical solutions of the model equations (2.11). Figures 15 and 16 show the response curves

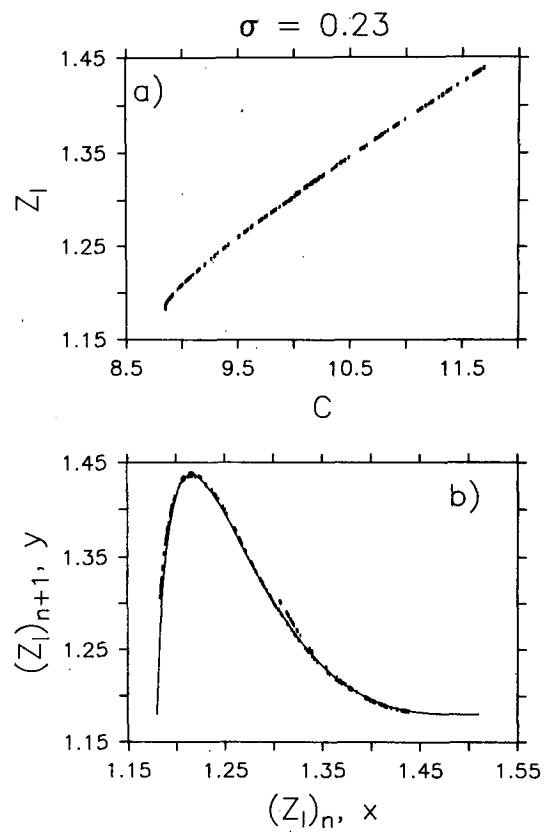

FIG. 10. (a) Intersections of solution at $\delta = 1$, $r = 0.02$, $\sigma = 0.23$ with half-plane $Z_R = 0$, $Z_I > 0.5$, $-\infty < C < \infty$; (b) solid line: Equation (4.1) with $\mu = 3.7$, $x_0 = 1.18$; dashes: Z_I-components of successive intersections of solution at $\delta = 1$, $r = 0.02$, $\sigma = 0.23$ with half-plane $Z_R = 0$, $Z_I > 0.5$, $-\infty < C < \infty$.

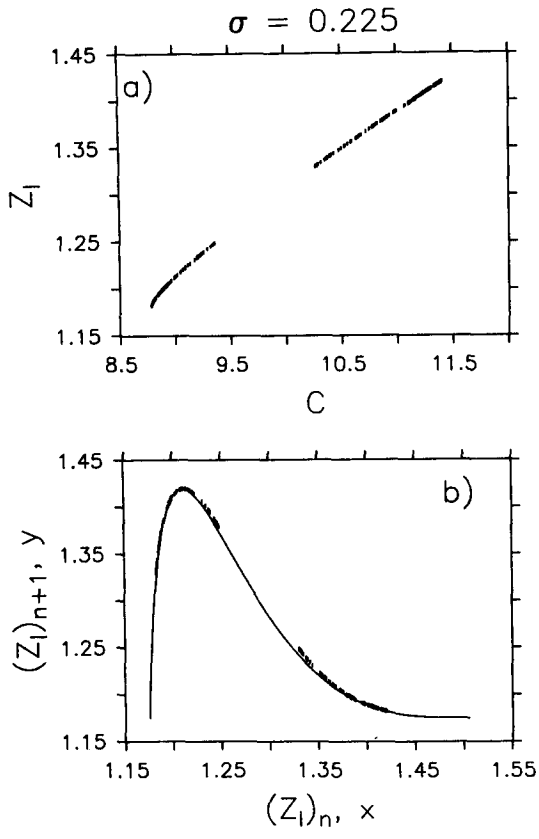

FIG. 11. (a) As in 10a except $\sigma = 0.225$; (b) As in 10b except $\sigma = 0.225$, $\mu = 3.64$, $x_0 = 1.175$.

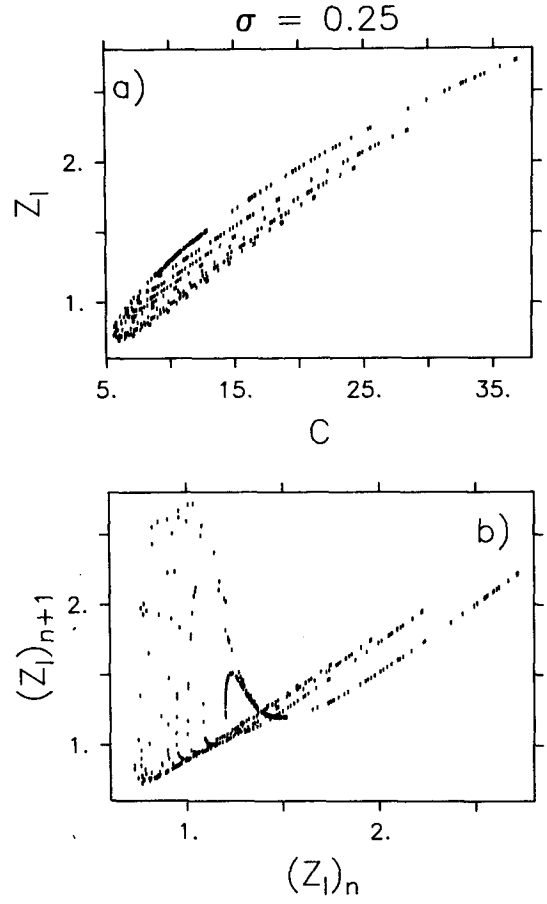

FIG. 13. (a) As in 10a except $\sigma = 0.25$; (b) successive intersection points as 10b except $\sigma = 0.25$.

from (3.16) and mean currents from (3.19), respectively, corresponding to parameter values $\tau = \epsilon^3 = 0.01$, 0.2, 1.0, $\delta = 0.5$ and $\hat{r} = \epsilon^2 r = \epsilon^2$ (0.1462, 0.2924), and the results of numerical integrations of (2.11), which are plotted as crosses joined by lines. At $\tau = 0.2$, $\hat{r} = 0.05$, 0.1; this forcing and the latter friction correspond to the parameter values suggested by the scaling arguments in section 2. The peak in amplitude near

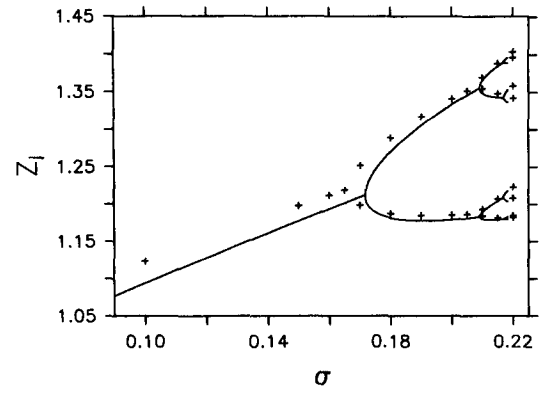

FIG. 12. Periodic points of Eq. (4.1) (solid line) and intersections of periodic orbits of numerical solutions with half plane (+) versus σ.

resonance remains in all cases but is distorted. As predicted by the perturbation solution, multiple equilibria exist for $r = 0.1462$ but not $r = 0.2924$. In all cases the prediction of negative mean current is verified. The agreement between mean current magnitudes is very good, in fact much better than that between the oscillation amplitudes. The numerical results indicate that, in contrast to the perturbation result, the solution with larger mean current at $\hat{r} = 0.05$, $\omega = 1.3$, actually has smaller amplitude. In fact, the mean flow of this solution is larger in magnitude than the amplitude: the time-varying current never becomes positive. In physical units, the numerical solutions indicate a mean flow of up to 4.5 cm s^{-1}, which compares well with results from recent numerical models that include more realistic topography (Haidvogel and Brink, 1986).

Behavior corresponding to the limit cycles, period doubling, and chaos found numerically in the averaged equations was found for very small parameter values in the model equations. A set of integrations at $\tau = 10^{-2}$ ($\epsilon \approx 0.2$), $\hat{r} = 10^{-3}$, $\delta = 1$ and various ω yielded periodic amplitude modulations, corresponding to the limit cycle observed near the Hopf bifurcation in the averaged

equations, but no period doubling or chaos. A set at $\tau = 10^{-3}$ ($\epsilon = 0.1$), $\hat{r} = 2 \times 10^{-4}$, $\delta = 1$ yielded chaotic amplitude modulation. At the parameter values suggested as physically relevant, we have not observed the complicated solutions that occur in the averaged equations. However, since the model is highly idealized, precise estimates of relevant parameter values are impossible to make; determining the range of behavior exhibited by the system is more important. The analysis demonstrates that on long time scales in an idealized model, continental slope flow may respond irregularly to weak wind forcing.

5. Flow structure

In this section we discuss the dependence of the maximum mean current (3.20) on dimensional parameters, give a physical interpretation of the short ($2\pi/\omega$) period oscillations, and examine the structure of the streamfunction and particle trajectories associated with the solutions of (3.10).

The maximum (over σ, for given τ, $\hat{r}$, and δ) mean current (3.20) may be expressed in dimensional variables as

$$[U']'_{0,\max} = -\left\{ \frac{\left(\frac{dh'}{dy'}\right)^3 \left(\frac{\delta'}{L}\right)^2}{\left[\left(\frac{dh'}{dy'}\right)^2 + \left(\frac{\delta'}{L}\right)^2\right]^3} \right\} \left(\frac{D}{L}\right)^2 \left(\frac{D}{\delta_E}\right)^2 \left(\frac{u_*}{fD}\right)^3 u_*, \tag{5.1}$$

where $u_* = (|\tau^{x'}|/\rho)^{1/2}$ and the other parameters are as in section 2. The last two factors multiplying u_* indicate that the efficiency of mean current generation increases as the inverse square of the bottom Ekman layer depth and the cube of the wind stress penetration scale. The second factor indicates that, for a given alongshore topographic aspect ratio δ'/L, the generation efficiency increases as the square of the fluid depth to topography length aspect ratio, so that short-wavelength topography generates greater mean currents. This is consistent with the numerical results of Haidvogel and Brink (1986). The first factor is principally related to the frequency of the inviscid oscillations and depends on both the shelf-slope dh'/dy' and the topographic aspect ratio δ'/L. To illustrate the dependence on this factor, we plot in Fig. 17 contours of the mean current (5.1) as a function of dh'/dy' and δ'/L, with the other parameters held constant at their values from section 2 ($D = 250$ m, $L = 5$ km, $\delta_E = 10$ m, $u_* = 1$ cm s^{-1}, $f = 10^{-4}$ s^{-1}). Mean flow generation is most efficient when the shelf slope and alongshore slope are comparable, and efficiency increases toward smaller slopes, which correspond to lower frequencies.

At first order, the solutions of (3.10) represent linear inviscid unforced oscillations whose (slowly varying) amplitude is determined by weak forcing, friction, and nonlinearity. The inviscid unforced system (3.6) is

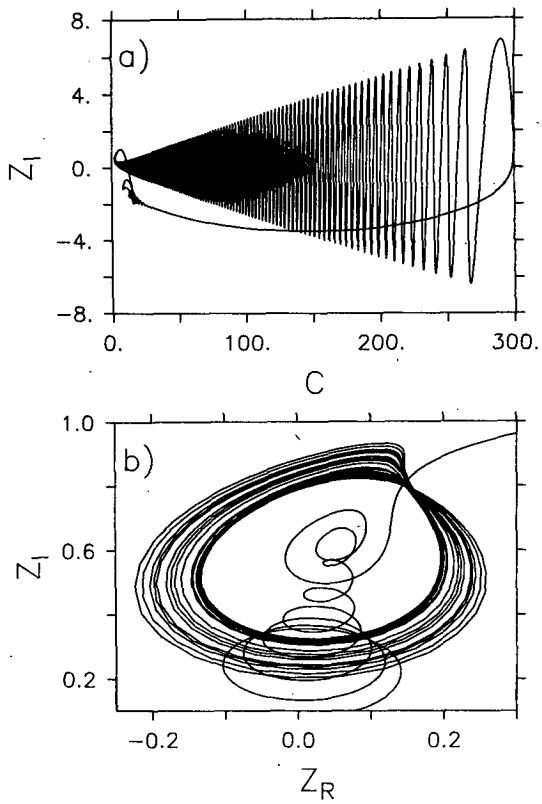

FIG. 14. Numerical solutions at $\delta = 1.1547$, $r = 0.02$, $\sigma = -0.225$. (a) Limit cycle; (b) chaotic attractor and portion of limit cycle.

Hamiltonian. The Hamiltonian function for the linear oscillations may be obtained from (3.6) by dropping the cubic and quartic terms and setting $G = 0$. These oscillations may be understood as the combination of a shelf wave, with balance $\phi_{xxt} = -\phi_x$ in (2.10b), and a wave due to the topographic variations, with balance $dU/dt = \langle \phi_x g \rangle$ and $\phi_{xxt} = -Ug_x$ in (2.10). (Rhines and Bretherton, 1973, treat a linear problem with similar oscillations.) When the cross-shelf flow is uncorrelated with the alongshore topography, there is no wave drag [$\phi_2 = 0$ in (2.11)]. Propagation of the shelf wave and vortex stretching by alongshore flow across the ridges create a topographic wave ($\phi_2 \neq 0$). Wave drag decelerates the alongshore flow, then accelerates it in the opposite direction. The shelf wave propagates until the cross-shelf flow is again uncorrelated with the alongshore topography, the wave drag vanishes, and the alongshore flow reaches its opposite maximum. The pattern repeats with alternating sign. Alongshore advection of the cross-shelf flow gives nonlinear coupling.

The streamfunction defined by (2.9), (2.12), (3.18) and the steady solutions (3.16), (3.17) may be written

$$\psi = \epsilon a_0 \psi_1 + \epsilon^2 a_0^2 \psi_2 + O(\epsilon^3), \tag{5.2}$$

where

$$\psi_1 = \left(-y + \frac{\sqrt{2}}{\delta}\cos x\right)\cos\Theta - \frac{\sqrt{2}}{\delta}\omega_0 \sin x \sin\Theta, \tag{5.3}$$

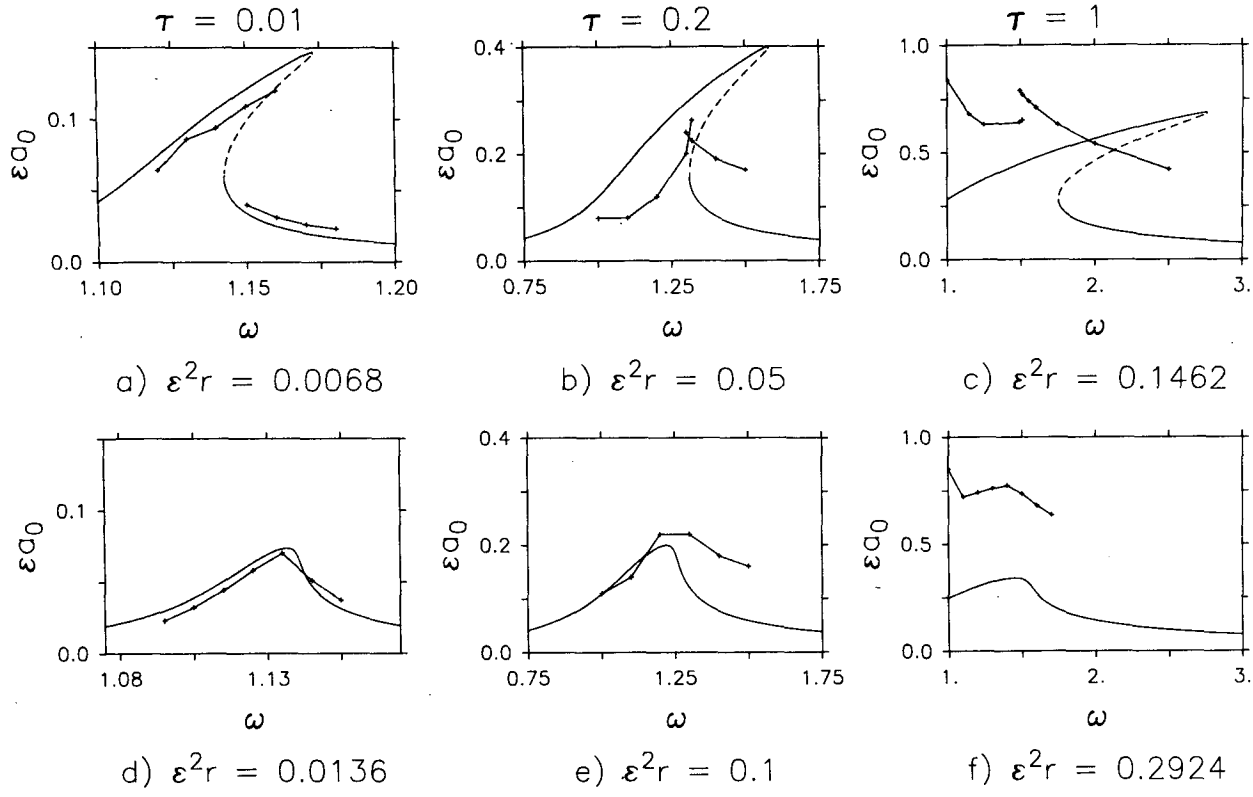

FIG. 15. Response curves (solid line: stable; dashed line: unstable) and amplitude of numerical solutions of Eq. (2.11) (-+-) versus frequency $\delta = 0.5$. (a) $\tau = 0.01$, $\hat{r} = 0.0068$; (b) $\tau = 0.2$, $\hat{r} = 0.05$; (c) $\tau = 1.0$, $\hat{r} = 0.1462$; (d) $\tau = 0.01$, $\hat{r} = 0.0136$; (e) $\tau = 0.2$, $\hat{r} = 0.1$; (f) $\tau = 1.0$, $\hat{r} = 0.2924$.

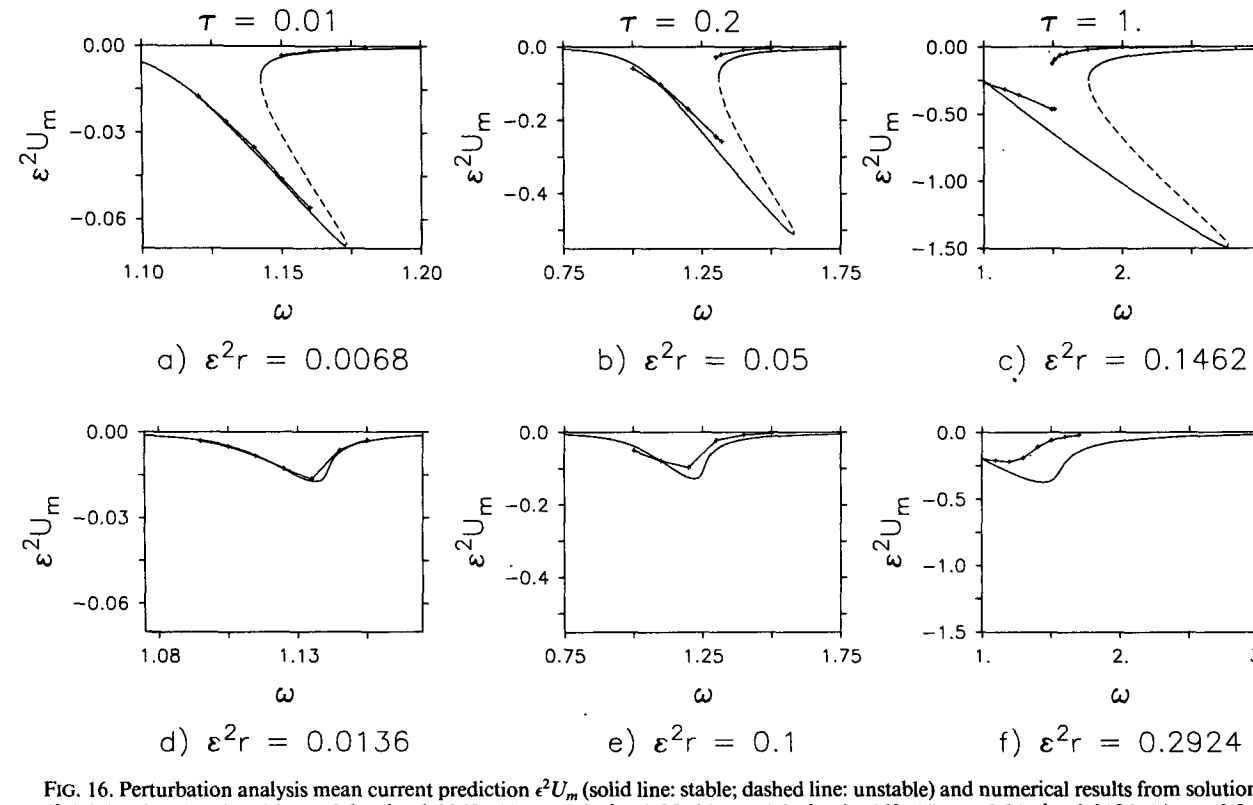

FIG. 16. Perturbation analysis mean current prediction $\epsilon^2 U_m$ (solid line: stable; dashed line: unstable) and numerical results from solutions to (2.11) (-+-) at $\delta = 0.5$. (a) $\tau = 0.01$, $\hat{r} = 0.0068$; (b) $\tau = 0.2$, $\hat{r} = 0.05$; (c) $\tau = 1.0$, $\hat{r} = 0.1462$; (d) $\tau = 0.01$, $\hat{r} = 0.0136$; (e) $\tau = 0.2$, $\hat{r} = 0.1$; (f) $\tau = 1.0$, $\hat{r} = 0.2924$.

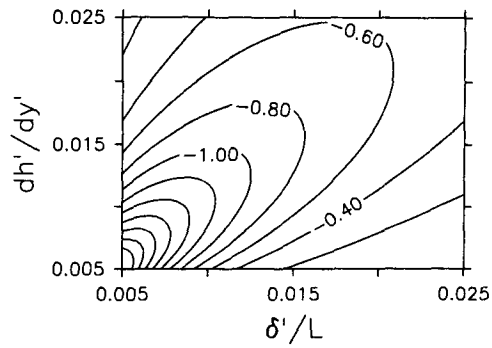

FIG. 17. Dependence of maximum mean current (5.1) on shelf slope (dh'/dy') and topographic amplitude (δ'/L). Values in cm s^{-1}.

$$\psi_2 = \frac{1}{\omega_0^2\delta^2}y + \frac{\sqrt{2}}{\delta}\left(\frac{1}{2}+\frac{1}{\omega_0^2}\right)\cos x + \left[\frac{1}{4\omega_0^2}y - \frac{\sqrt{2}}{\delta}\left(1+\frac{1}{\omega_0^2}\right)\cos x\right]\cos 2\Theta + \frac{\sqrt{2}}{2\omega_0\delta}\sin x \sin 2\Theta, \quad (5.4)$$

$$\Theta = \omega t + \gamma_0. \quad (5.5)$$

In Fig. 18, we display the cross-shelf velocities ψ_{1x} and ψ_{2x} versus x at $\delta = 0.5$. Phase propagation is toward negative x in both. The first-order part is nearly a simple traveling sinusoid. Its sign reverses every half period. The second-order part oscillates at twice the forcing frequency about a nonzero time mean that is proportional to $\sin x$.

The alongshore velocities $-\psi_{1y}$ and $-\psi_{2y}$ do not vary in x. The first-order part oscillates at the forcing frequency. The second-order part oscillates at twice the forcing frequency about a negative mean.

For the steady-state oscillations, the Lagrangian trajectories are easily obtained by integrating $dx/dt = -\psi_y(t)$ and $dy/dt = \psi_x[x(t), t]$ with respect to time. These trajectories are

$$x(t) = c_1 + \epsilon^2 U_{m_0} t + \epsilon\frac{a_0}{\omega_0}\sin\Theta + \epsilon^2\frac{\delta^2}{2}U_{m_0}\sin 2\Theta + O(\epsilon^3 t) \quad (5.6)$$

and

$$y(t) = c_2 - \sqrt{2}\delta\cos X + \frac{\epsilon a_0\sqrt{2}}{\omega_0\delta}[\cos X\cos\Theta - \omega_0\sin X\sin\Theta] + \epsilon^2\frac{\sqrt{2}\delta}{4}U_{m_0}\left(\omega_0+\frac{2}{\omega_0}\right)\sin X\sin 2\Theta + O(\epsilon^3 t), \quad (5.7)$$

where c_1 and c_2 are constants of integration, and

$$X \equiv [x(t)]^t = c_1 + \epsilon^2 U_{m_0} t + O(\epsilon^3 t) \quad (5.8)$$

represents the average x-position of a particle over a forcing period. The trajectories are composed of quasi-periodic motion and a slow drift. The quasi-periodic motion represents oscillations on the forcing time scale modulated by sines and cosines of the average x-position over a forcing period (which changes on the time scale of the drift, $1/\epsilon^2$), and thus may appear complicated in spite of its near periodicity.

Mean Lagrangian drift is along isobaths. From (5.7), the average y-position of a particle over a forcing period is

$$Y = [y(t)]^t = c_2 - \sqrt{2}\delta\cos X + O(\epsilon^3 t, \epsilon^4). \quad (5.9)$$

Except for the small error term, (5.9) is exactly the equation for the isobaths, which is implicitly given by (2.2) with h and δ constant. Eulerian and Lagrangian means are equal in the alongshore but not the cross-shelf direction.

6. Discussion

The averaging analysis in section 3 shows that the model developed in section 2 for wind forced flow over topography on the continental slope predicts a negative

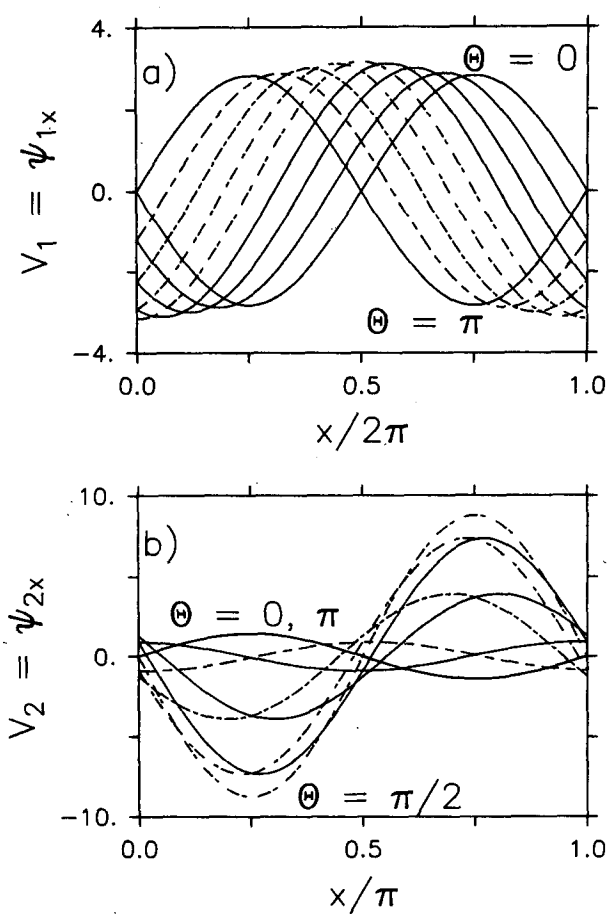

FIG. 18. Cross-shelf velocities at $\delta = 0.5$, for $\Theta = 0$, $\pi/8$, $\pi/4$, $3\pi/8$, π (solid lines); $\pi/2$, $5\pi/8$, $3\pi/4$, $7\pi/8$ (dashed lines) for (a) ψ_{1x}, (b) ψ_{2x}.

mean flow (that is, in the direction of topographic Rossby wave phase propagation) in response to weak near-resonant forcing with weak friction. The mean flow is negative regardless of the values of the scaled friction and frequency parameters and the height of the topography. This is a robust prediction. Low-frequency oscillations over short-wavelength topography with comparable alongshore and cross-shelf slopes generate mean flow most efficiently. The averaged equations have multiple equilibria, which correspond to multiple solutions with steadily oscillating currents in the model. To our knowledge, the existence of such multiple oscillatory states in a model of coastal currents is a new result.

The numerical solutions of the model equations in section 4b indicate that the negative mean flow prediction persists for parameter values that are suggested by physical arguments and are not asymptotically small. Qualitatively we may anticipate this, since the topographic lee wave resonance (where the drag should be most anisotropic) occurs at nondimensional alongshore velocity $U = 1$, whereas the averaging analysis requires $U = O(\epsilon)$, $\epsilon \ll 1$. The magnitude of the mean flow is comparable to the results of numerical models with more realistic topography (Haidvogel and Brink, 1986). The numerical solutions in section 4b also indicate that multiple steady oscillations persist for these larger parameter values.

The fact that a simple model of slope flow can have an irregular (chaotic) response to regular (periodic) forcing is of interest. Since Lorenz' (1963) hypothesis that aperiodic behavior of nonlinear deterministic systems could be important in interpreting the observed lack of periodicity in large-scale atmospheric flows, relatively few oceanographically motivated geophysical fluid models that exhibit such behavior have been studied. (For results of a general nature on baroclinic waves, see Pedlosky and Frenzen, 1980, and Pedlosky, 1981; for the atmospheric problem, see Lorenz, 1980.) This model suggests that the response of slope flow to atmospheric forcing may be irregular on long time scales. In this case, a linear analysis of ocean–atmosphere coupling over the slope could be misleading.

Our results stimulate several questions about the physical problem:

(1) What is the response to periodic forcing when the alongshore topography has a continuous wavenumber spectrum?

(2) How does the response change when the cross-shelf scales of the topographic variations are comparable to the alongshore scales?

(3) What is the response when the wind stress has a nonzero time mean and a continuous frequency spectrum?

(4) What is the effect of stratification?

(5) Would the chaotic response persist in a model with more degrees of freedom?

Question 4 is important because scaling arguments (section 2) indicate that short alongshore scales $L \approx 5$ km characterize the resonant barotropic topographic wave for typical alongshore velocities $U_0 \approx 10$ cm s^{-1}. Linear analyses of rotating stratified flow indicate that bottom-generated disturbances will have a vertical decay scale $O(fL/N)$, where N is the Brunt–Väisälä frequency. Over the continental shelf and slope, N typically ranges from 10^{-3} to 5×10^{-2} s^{-1}, which for $L \approx 5$ km gives vertical decay scales from 500 to 10 m. For the depth scale chosen here, $D \approx 250$ m, a barotropic analysis may be strictly appropriate on these small horizontal scales only if the stratification is weak. We believe the simplicity of our results is worth the price of the idealization. Moreover (as mentioned in section 2) the small-amplitude averaging analysis that yielded the mean current prediction (5.1) effectively considers topography much larger than the resonant scale. [One can see this from (2.10) by replacing $\cos x$ with $\alpha^{-1}\cos\alpha x$, $\alpha \ll 1$, in g and multiplying U and t by α, which yields (after Fourier expansion) equations equivalent to (2.11) with the small parameter α^3 multiplying the nonlinear terms.] On these larger scales, the barotropic analysis will be appropriate for stronger stratification (for example, $L \approx 25$ km and $N = 10^{-2}$ s^{-1} gives a vertical decay scale of 250 m). Consequently, (4) above leads naturally to the consideration of topography with many scales of variation, and brings us back to (1) and (2).

We see no reason to expect that the mean flow generation result will be qualitatively altered by the inclusion of more alongshore topographic modes, since the neglect of the direct nonlinear interaction of the wave modes follows from the hypothesis of slow cross-channel variation, not from the choice of single-mode topography. Simple models have proven useful in previous work on steady flow over topography. Charney and DeVore (1979) verified the existence of multiple equilibria that were predicted by their low-order model (equivalent to the equations of Hart 1979, but derived by truncation) by numerical integration of a grid point model. Davey (1980, 1981) found good agreement at small Rossby number (and at larger Rossby number, when mean zonal shear effects were included) between a quasi-linear theory of zonal flow over many-mode topography and a fully nonlinear numerical model.

If topography is considered that varies across the channel on scales that are large relative to the alongshore wavelength, our analysis indicates that the character of the response may depend on the cross-channel location, since the character of the solutions we obtained can depend on the parameter $\delta(y)$. Further study is required to determine how our results would be modified if variations in the solutions on shorter cross-channel scales were allowed.

The relation of chaotic solutions of low-order models to the behavior of systems with many degrees of freedom is currently an object of intense research interest

in many fields of physics. Curry et al. (1984) have numerically reexamined the convection problem from which Lorenz (1963) drew his exemplary equations, and found chaos in three but not in two dimensions at high resolution. Klein and Pedlosky (1986) have solved a two-layer quasi-geostrophic numerical model of baroclinically unstable waves and found that a truncated system overestimated the domain of chaotic behavior at moderate nonlinearity, but not at stronger nonlinearity. In general, the relation is not well understood. We do not feel that it is possible at present to predict whether chaotic behavior would be more or less prevalent if more modes were included in the present model. The above questions can only be answered by further research, in which the effect of relaxing our assumptions may be systematically explored.

Chaotic solutions of differential equations are of mathematical as well as physical interest. The asymptotic behavior that we have approximated by a one-dimensional map appears to be similar to a type studied by Rössler (1976) and Shaw (1981). The spiral type behavior in the solution of Fig. 9 resembles attractors examined by Arneodo et al. (1981, 1982) and related by them to the Rössler type and to results (Shil'nikov, 1965; see also Guckenheimer and Holmes, 1983, Chap. 6) on trajectories near a homoclinic orbit to a steady solution about which the linearized equations have oscillatory solutions that decay (or grow) at a certain rate. The steady solution that undergoes the Hopf bifurcation at p_3 may, for some parameter value, have such a homoclinic orbit. The existence of the large-amplitude limit cycle at $\delta = 1.1547$, $r = 0.02$ (Fig. 14), that passes close to the unstable steady solution and through the limit cycle associated with the Hopf bifurcation, supports this conjecture. Period doubling sequences have been related to the appearance of homoclinic tangencies (Guckenheimer and Holmes, 1983, Chap. 6); whether such a tangency is associated with the observed period doubling in the averaged equations is not clear. Chaotic solution sets also arise when a separatrix bifurcates under perturbation to a homoclinic orbit representing a transverse intersection of the unstable and stable manifolds of an invariant set. The method of Melnikov (1961) may be used to test for the existence of this bifurcation. In our case, both the inviscid unforced equations and the inviscid averaged equations possess separatrices. Application of an extension of the Melnikov method (Holmes and Marsden, 1982; Robinson, 1983; Holmes, 1986) to these equations is under study.

Acknowledgments. This research was supported for R.M.S. by the Office of Naval Research under Contract N0014-84-C-0218 and for J.S.A. by the National Science Foundation under Grants OCE-8411613 (Coastal Ocean Dynamics Experiment—CODE) and OCE-8405232 ("SuperCODE"). Computational resources were supported by NSF Grant OCE-8541635. The authors thank P. Newberger and J. Dawson for assistance with the computations and F. Beyer for typing the manuscript.

APPENDIX A

Averaging

First we show that with the scaling (3.7), all solutions of (3.3) eventually have $U, F = O(\epsilon)$, $G = O(\epsilon^2)$. From (2.11) and (3.2b), we obtain

$$\frac{dE}{dt} = -2\epsilon^2 rE + \epsilon^3 U\cos\omega t. \tag{A1}$$

If $E^{1/2} \geq \sqrt{2}\epsilon/r$, it follows that

$$\frac{d}{dt}(e^{\epsilon^2 rt}E) = -\epsilon^2 e^{\epsilon^2 rt}(rE - \epsilon U\cos\omega t) \leq 0, \tag{A2}$$

since $E \geq \frac{1}{2}U^2 \geq 0$. Integration of the differential inequality (A2) gives

$$E(t) \leq E(t=0)e^{-\epsilon^2 rt}, \tag{A3}$$

so for $r > 0$, all solutions are order ϵ after finite time ($t \geq t_1 = \epsilon^{-2}\log\epsilon^{-2}$). Substituting $U = \epsilon U_1$ and $G = \epsilon G_1$ (at $t = 0$, for convenience) in (3.3c) and integrating, we obtain

$$|G_1| \leq |G_1(t=0)e^{-\epsilon^2 rt}| + \epsilon|4r^{-2}(1 - e^{-\epsilon^2 rt})| + \epsilon^2|(\omega^2 + \epsilon^4 r^2)^{-1}[\omega\sin\omega t + \epsilon^2 r(\cos\omega t - e^{-\epsilon^2 rt})]| \tag{A4}$$

so G_1 will itself be order ϵ after finite time ($t \geq \frac{1}{2}t_1$), and G will be order ϵ^2 after finite time ($t \geq \frac{3}{2}t_1$).

The linear inviscid unforced solutions of (3.3) and variation of constants suggest the use of the time-dependent transformation

$$\begin{pmatrix} A \\ \bar{A} \\ B \end{pmatrix} = W^{-1}\begin{pmatrix} U_1 \\ F_1 \\ G_2 \end{pmatrix}, \quad W = \begin{pmatrix} \Omega & \bar{\Omega} & 0 \\ i\omega\Omega & -i\omega\bar{\Omega} & 0 \\ 0 & 0 & 1 \end{pmatrix}, \tag{A5}$$

where

$$\Omega = e^{i\omega t}, \tag{A6}$$

overbar denotes complex conjugate and $(U, F, G) = (\epsilon U_1, \epsilon F_1, \epsilon^2 G_2)$. After transformation and the use of (3.7), the equations for the slowly varying complex amplitude A and real quantity B are

$$\frac{dA}{dt} = \epsilon\left[-\frac{\bar{\Omega}}{2i\omega}B + \frac{3\bar{\Omega}}{4i\omega}(\Omega A + \overline{\Omega A})^2\right] + \epsilon^2\left[-rA - i\sigma(A + \bar{\Omega}^2\bar{A}) + \frac{1}{4}(1 + \bar{\Omega}^2) + \frac{1}{2i\omega}(A + \bar{\Omega}^2\bar{A})B - \frac{\bar{\Omega}}{4i\omega}(\Omega A + \overline{\Omega A})^3\right], \tag{A7}$$

$$\frac{dB}{dt} = \epsilon\left[-\frac{1}{2}(\Omega + \bar{\Omega})\right] + \epsilon^2\left[-rB - \frac{1}{2}r(\Omega A + \overline{\Omega A})^2 + \frac{1}{2}(\Omega + \bar{\Omega})(\Omega A + \overline{\Omega A})\right]. \tag{A8}$$

These are in the appropriate form for averaging.

The method of averaging allows explicit calculation

of error estimates, and theorems exist proving the closeness of perturbation solutions to the true solutions (Bogoliubov and Mitropolsky, 1961; Hale, 1969; Sanders and Verhulst, 1985). We outline the method that we will follow for second-order averaging, using the notation of Holmes and Holmes (1981). See Perko (1969) for details on higher-order averaging.

Given a set of n ordinary differential equations

$$\frac{dx}{dt} = \epsilon f(x,t) + \epsilon^2 g(x,t) \tag{A9}$$

where $x = (x_1, \cdots, x_n)$, $f = (f_1, \cdots, f_n)$, $g = (g_1, \cdots, g_n)$, ϵ is a small parameter, and f and g are T-periodic in t, decompose f and g into time-averaged and periodic parts according to

$$\phi^0(x) = \frac{1}{T}\int_0^T \phi(x,t)dt,$$

$$\phi^1(x,t) = \phi(x,t) - \phi^0(x). \tag{A10}$$

Consider a transformation

$$x = y + \epsilon u(y,t) + \epsilon^2 v(y,t), \tag{A11}$$

where the u and v are to be determined later but must be periodic in t with $u^0 = v^0 = 0$. Substitute (A11) into (A9). Note that

$$\frac{dx}{dt} = [I + \epsilon Du + \epsilon^2 Dv]\frac{dy}{dt} + \epsilon\frac{\partial u}{\partial t} + \epsilon^2\frac{\partial v}{\partial t}, \tag{A12}$$

where $D\phi = (\partial\phi_i/\partial y_j)$ is the matrix of partial derivatives, and expand f and g in Taylor series,

$$f(x,t) = f(y,t) + \epsilon Df(y,t,)u(y,t) + O(\epsilon^2),$$
$$g(x,t) = g(y,t) + O(\epsilon). \tag{A13}$$

Also note that

$$[I + \epsilon Du + \epsilon^2 Dv]^{-1} = I - \epsilon Du + O(\epsilon^2), \tag{A14}$$

so

$$\frac{dy}{dt} = \epsilon\left(f - \frac{\partial u}{\partial t}\right) + \epsilon^2\left[g + Dfu + Du\left(f - \frac{\partial u}{\partial t}\right) - \frac{\partial v}{\partial t}\right] + O(\epsilon^3). \tag{A15}$$

Now choose u and v to eliminate the periodic part of the right-hand side at each order, by setting

$$\frac{\partial u}{\partial t} = f^1, \tag{A16}$$

$$\frac{\partial v}{\partial t} = g^1 + Df^0 u - Duf^0, \tag{A17}$$

and integrating. Then the (truncated) averaged equations are

$$\frac{dz}{dt} = \epsilon f^0(z) + \epsilon^2[g^0(z) + (Df^1 u)^0], \tag{A18}$$

where higher-order terms have been dropped and we denote the solution by z to distinguish it from the exact solution y of (A15). Error estimates come from f and g and their derivatives. If f^0 vanishes, as it will in our case, and f is twice and g once continuously differentiable, it follows that

$$x = z + \epsilon u(z,t) + O[\epsilon^2, \epsilon(e^{\epsilon^2 Lt} - 1)], \tag{A19}$$

where $\epsilon^2 L$ is a Lipschitz constant for the right-hand side of (A18) (Sanders and Verhulst, 1985). Here the initial conditions for (A18) are just those for (A15), implicitly defined by (A11) at $t = 0$. A hyperbolic steady solution of (A18) corresponds, for sufficiently small ϵ, to a periodic solution of the original equations. These and the solutions approaching them asymptotically are approximated to $O(\epsilon^2)$ uniformly for $0 \leq t < \infty$. (In this case the second error estimate in (A19) does not apply.)

For the set (A7, A8), the first order part of the transformation (A11) is

$$u_1 = -\frac{3A^2}{4\omega^2}\Omega + \frac{1}{2\omega^2}(3A\bar{A} - B)\bar{\Omega} + \frac{\bar{A}^2}{4\omega^2}\bar{\Omega}^3, \quad u_2 = \bar{u}_1, \tag{A20a,b}$$

$$u_3 = -\frac{1}{2i\omega}(\Omega - \bar{\Omega}). \tag{A21}$$

The averaged equations are (3.10) with the variables defined in (3.8) and (3.9), that is, we rename A and B to Z and C when truncating to obtain (3.10).

From (A19) and (3.8), it follows that the error in using solutions of (3.10) to approximate solutions of (3.3) is $O[\epsilon^3, \epsilon^2(e^{\epsilon^2 Lt} - 1)]$. For hyperbolic steady solutions of (3.10), the error is $O(\epsilon^3)$ for $0 \leq t < \infty$. In (3.8c), the error term is multiplied by ϵ. For unsteady solutions of (3.10), (3.12) will only hold on time scales less than ϵ^{-2}, since the limit as $\epsilon \to 0$ of ϵ^{-2} times the error terms only vanishes on time scales less than ϵ^{-2}.

APPENDIX B

Boundedness of Solutions of the Averaged Equations

If $r = 0$, the averaged equations (3.14) reduce to a Hamiltonian system. The Hamiltonian function is

$$H(Z_R, Z_I) = \frac{1}{2}(\sigma - b_1 J)(Z_R^2 + Z_I^2) - \frac{1}{4}\left(\frac{2b_1}{k} + b_2\right)(Z_R^2 + Z_I^2)^2 + \frac{1}{2}kZ_I, \tag{B1}$$

and the quantity

$$J = C - \frac{1}{k}(Z_R^2 + Z_I^2),$$

is conserved.

If $r > 0$, inequalities similar to (A3) and (A4) may be derived as follows to show that all attracting sets are

contained in a cylinder centered at the origin. If $Z_R^2 + Z_I^2 \geq k^2/r^2$, then by (3.14a, b),

$$\frac{d}{dT_2}[(Z_R^2 + Z_I^2)e^{rT_2}] = -e^{rT_2}[r(Z_R^2 + Z_I^2) - kZ_R] \leq 0, \tag{B2}$$

so

$$Z_R^2 + Z_I^2 \leq (Z_R^2 + Z_I^2)\,(T_2 = 0)e^{-rT_2} \tag{B3}$$

and in finite time,

$$Z_R^2 + Z_I^2 \leq k^2/r^2. \tag{B4}$$

Once (B4) holds, (3.14) may be integrated to yield

$$|C| \leq |C\,(T_2 = 0)|e^{-rT_2} + \frac{k(1+k)}{r^2}(1 - e^{-rT_2}) \tag{B5}$$

(for convenience in notation we assume that (B4) holds at $T_2 = 0$). In finite time,

$$|C| \leq \frac{Sk(1+k)}{r^2}, \tag{B6}$$

where S is any number greater than 1.

APPENDIX C

Stability of Steady Solutions

The eigenvalues of the linearization of (3.14) at a steady solution determine its stability (if none have zero real part): all real parts negative means stable, any positive means unstable. The eigenvalues are the roots of the characteristic polynomial

$$\lambda^3 + a\lambda^2 + b\lambda + c = 0, \tag{C1}$$

where the coefficients are

$$a = 3r, \tag{C2a}$$

$$b = 3r^2 + (\sigma - \alpha a_0^2)(\sigma - \Gamma a_0^2), \tag{C2b}$$

$$c = r[r^2 + (\sigma - \alpha a_0^2)(\sigma - 3\alpha a_0^2)], \tag{C2c}$$

$$\Gamma = \frac{1}{16\delta^2\omega_0^3}(32 - 24\delta^2 - 5\delta^4). \tag{C3}$$

A necessary and sufficient condition for stability is that the coefficients satisfy (Birkhoff and MacLane, 1953, Chap. V.7)

$$a > 0, \quad b > 0, \quad c > 0, \quad ab > c. \tag{C4}$$

(Note that the second is implied by the other three.) Since $r > 0$, the first condition is always satisfied. From (C2c) and (3.16),

$$c = rP'(a_0^2) \tag{C5}$$

so the sign of c is just the sign of $P'(a_0^2)$. From (3.16), $P > 0$ and $P' > 0$ for large a_0^2, so $c > 0$ at the largest solution of (3.16) if (3.16) has either one or three solutions. Thus, since P is cubic, $c < 0$ precisely for the intermediate of the multiple equilibria, and this solution is always unstable when it exists.

Letting

$$Q(a_0^2) = ab - c, \tag{C6}$$

and substituting (C2a–c) and (3.21a), we obtain

$$Q(a_0^2) = r\left[6r^2 + \frac{2k^2}{a_0^2} \pm (5\alpha - 3\Gamma)a_0^2\left(\frac{k^2}{a_0^2} - r^2\right)^{1/2}\right], \tag{C7}$$

where the choice of sign corresponds to that in (3.21a). From (3.18) and (C3),

$$5\alpha - 3\Gamma = \frac{1}{\delta^2\omega_0^3}(2\delta^2 - 1). \tag{C8}$$

For $0 < \delta < 1/\sqrt{2}$, Q is positive on the left branch. For $\delta > 1/\sqrt{2}$, Q is positive on the right branch. In these two cases, stability depends only on the sign of c. If multiple equilibria exist, the intermediate solution is unstable; other solutions are stable.

It remains to investigate the stability of the right branch for $0 < \delta < 1/\sqrt{2}$ and the left branch for $\delta > 1/\sqrt{2}$. Further progress requires solution of cubic and higher order polynomials. We give analytical results for small r here, and display numerical results for general r in Figs. 2–5.

Consider $r \ll 1$. First, set $c = 0$ and solve for the points of vertical tangency. [By (3.25), multiple equilibria exist for small r except at $\delta = 2/\sqrt{3}$.] Between these points is the unstable intermediate solution. Multiple solutions may occur on the right branch for $\delta < 2/\sqrt{3}$ and on the left branch for $\delta > 2/\sqrt{3}$. In either case, $c = 0$ means

$$\frac{k^2}{a_0^2} - 2|\alpha|a_0^2\left(\frac{k^2}{a_0^2} - r^2\right)^{1/2} = 0, \tag{C9}$$

so the vertical tangents occur at

$$a_{01}^2 = \left(\frac{k^2}{4\alpha^2}\right)^{1/3} + O(r^2), \tag{C10}$$

$$a_{02}^2 = \frac{k^2}{r^2} - \frac{r^4}{4\alpha^2k^2} + O(r^{10}), \tag{C11}$$

where the corresponding frequencies are

$$\sigma_1 = 3\left(\frac{\alpha k^2}{4}\right)^{1/3} + O(r^2), \tag{C12}$$

$$\sigma_2 = \frac{\alpha k^2}{r^2} + \frac{r^4}{4\alpha k^2} + O(r^{10}). \tag{C13}$$

Second, find the zeros of Q. The solutions are

$$a_{03}^2 = \left[\frac{4k^2}{(5\alpha - 3\Gamma)^2}\right]^{1/3} + O(r^2), \tag{C14}$$

$$a_{04}^2 = \frac{k^2}{r^2} - \frac{64r^4}{k^2(5\alpha - 3\Gamma)^2} + O(r^{10}), \tag{C15}$$

where the corresponding frequencies are

$$\sigma_3 = \frac{3}{2}(\Gamma - \alpha)\left[\frac{4k^2}{(5\alpha - 3\Gamma)^2}\right]^{1/3} + O(r^2), \quad \text{(C16)}$$

$$\sigma_4 = \alpha\frac{k^2}{r^2} - \left(1 + \frac{8\alpha}{5\alpha - 3\Gamma}\right)\frac{8r^4}{k^2(5\alpha - 3\Gamma)} + O(r^{10}) \quad \text{(C17)}$$

(where these values are taken on the right branch for $0 < \delta < 1/\sqrt{2}$ and on the left branch for $\delta > 1/\sqrt{2}$). Differentiating Q along the resonance curve [i.e., substituting for σ using (3.21a) and differentiating with respect to a_0^2] and evaluating at a_{03}^2 gives

$$Q'(a_{03}^2) = \frac{2rk^2}{a_{03}^4}\left[-1 \pm (5\alpha - 3\Gamma)\frac{ka_0}{4}\right] + O(r^3), \quad \text{(C18)}$$

which is less than zero on the right branch if $0 < \delta < 1/\sqrt{2}$ and on the left branch if $\delta > 1/\sqrt{2}$. Since also

$$Q(a_0^2 = k^2/r^2) = 8r^3 > 0, \quad \text{(C19)}$$

Q is in fact negative precisely between its zeros, and the solution is unstable there.

When $1/\sqrt{2} < \delta < \sqrt{2}$, the bifurcation at p_3 is a Hopf bifurcation for small r. At p_3, for small r,

$$a = O(r), \quad b = O(1), \quad c = O(r), \quad \text{(C20)}$$

so the roots are

$$\lambda_{1,2} = \pm ib^{1/2} + \frac{1}{2}(cb^{-1} - a) + O(r^2),$$

$$\lambda_3 = -cb^{-1} + O(r^2). \quad \text{(C21)}$$

Here $b > 0$, since $1/\sqrt{2} < \delta < \sqrt{2}$ and

$$b(a_{03}^2) = \frac{k^2}{4a_{03}^2}\left(\frac{4 - \delta^4}{2\delta^2 - 1}\right) + O(r^2), \quad \text{(C22)}$$

and $c > 0$ except at the unstable intermediate amplitude solutions. The condition that Q have a simple zero at p_3 follows from (C18).

The points of bifurcation to instability, $p_i = (\sigma_i, a_{0i}^2)$, $i = 1, \cdots, 4$, are functions of r and δ. Equality relations between them (e.g., $p_3 = p_4$ or $\sigma_1 = \sigma_3$) implicitly define curves (bifurcation sets) that divide the (δ, r) plane into regions in which the response curves are qualitatively similar. Figure 2 displays these regions and their boundaries as given by numerical computation. For each point there is a response curve giving the amplitude as a function of frequency. (One from each region is shown in Fig. 3.) The regions (except the small region VIII) are numbered with increasing δ at small r. The asymptotic results above allow analytic definition of the regions and bifurcation sets in the limit of small r.

In region I, there is one stable steady solution at each σ. The bounding curves are (3.24a) between regions I and II and between I and X [henceforth designated by (I, II; I, X)] and $p_3 = p_4$ (I, V). This region vanishes in the limit of small r.

In region II, there are multiple equilibria, two stable and the intermediate unstable, between σ_1 and σ_2. The unstable solution is on the right branch. Elsewhere there is one stable fixed point. The bounding curves are (3.24a) (I, II) and $p_3 = p_4$ (II, III). The interval of instability between p_3 and p_4 is subsumed within that between p_1 and p_2. In the limit of small r, region II occupies $0 < \delta < 1/\sqrt{2}$.

In region III, there are multiple equilibria between σ_1 and σ_2. The unstable intermediate solutions are on the right branch. Also, the largest of the three steady solutions (which is on the left branch) is unstable between σ_3 and σ_4. The bounding curves are $p_3 = p_4$ (II, III) and $\sigma_3 = \sigma_1$ (III, IV). In the limit of small r, region III occupies $1/\sqrt{2} < \delta \leqslant 0.805$.

In region IV, the instability of the left branch extends to the left of the σ-interval where multiple equilibria exist. Thus no stable equilibria exist between σ_3 and σ_1. The bounding curves are (3.24a) (IV, V), $p_3 = p_4$ (II, IV), and $\sigma_3 = \sigma_1$ (III, IV). In the limit of small r, region IV occupies $0.805 \leqslant \delta < 2/\sqrt{3}$.

In region V, there are no multiple equilibria, and between σ_3 and σ_4, the single steady solution is unstable. The bounding curves are (3.24a) (IV, V; V, VI; V, VIII) and $p_3 = p_4$ (I, V). In the limit of small r, region V shrinks to the point $\delta = 2/\sqrt{3}$, where $\alpha = 0$.

In region VI, there are multiple equilibria between σ_2 and σ_1, Now $\alpha < 0$, so they occur for $\sigma < 0$; the unstable intermediate solution is on the left branch. The inequality $a_{03} < a_{01} < a_{02} < a_{04}$ holds, so there is also instability at large and small amplitude, and an interval exists ($\sigma_3 < \sigma < \sigma_4$) in which there are no stable solutions. The bounding curves are (3.24a) (V, VI), $\sigma_2 = \sigma_3$ (VI, VII), and, in the extreme upper right, $p_2 = p_4$ (VI, VIII). (In fact there is a separate region along the lower right-hand boundary of region VI where $\sigma_2 < \sigma_3 < \sigma_4$, $a_{02} < a_{04}$, and no stable solutions exist for $\sigma_3 < \sigma < \sigma_4$; it is too thin to depict in Fig. 2.) In the limit of small r, region VI vanishes.

In region VII, the same inequalities as in VI hold, except that $\sigma_4 < \sigma_3$, so there is at least one stable solution everywhere. Only the large-amplitude solution is stable between σ_3 and σ_1, and it is unstable between σ_2 and σ_4. The bounding curves are $\sigma_3 = \sigma_4$ (VI, VII) and $p_2 = p_4$ (VII, IX). In the limit of small r, region VI occupies $2/\sqrt{3} < \delta < (\sqrt{6} - 1)^{1/2} \approx 1.203$.

In region VIII, the same inequalities as in VI hold, except that $a_{04} < a_{02}$, so the interval in which there are no stable solutions is $\sigma_3 < \sigma < \sigma_2$. The bounding curves are (3.24a) (V, VIII), $p_2 = p_4$ (VI, VIII), and $\sigma_2 = \sigma_3$ (VIII, IX). This region is small. For $r \leqslant 0.09$, it vanishes.

In region IX, the small-amplitude solution (as well as the intermediate) is unstable, and at least one stable solution exists everywhere, since $\sigma_2 < \sigma_3$. Only the large amplitude solution is stable between σ_3 and σ_1. The bounding curves are $p_2 = p_4$ (VII, IX), $\sigma_2 = \sigma_3$ (VIII, IX), and $p_1 = p_3$ (IX, X). In the limit of small r, region IX occupies $(\sqrt{6} - 1)^{1/2} < \delta < \sqrt{2}$.

In region X, there are multiple equilibria for $\sigma_2 < \sigma < \sigma_1$; only the intermediate solution is unstable. The inequality $a_{01} < a_{03} < a_{04} < a_{02}$ holds everywhere, so

as in region I, the interval of instability between p_3 and p_4 is subsumed within that between p_1 and p_2. The bounding curves are $p_3 = p_1$ (IX, X) and (3.24a) (I, X). In the limit of small r, region X occupies $\delta > \sqrt{2}$. As $\delta \to \infty$, the bounding curve (3.24a) approaches $r = 0$ as $\delta^{-1/3}$.

REFERENCES

Arneodo, A., P. Coullet and C. Tresser, 1981: Possible new strange attractors with spiral structure. *Commun. Math. Physics,* **79,** 573–579.

——, —— and ——, 1982: Oscillators with chaotic behavior: An illustration of a theorem by Shil'nikov. *J. Stat. Phys.,* **27**(1), 171–182.

Birkhoff, G., and S. MacLane, 1953: *A Survey of Modern Algebra.* Macmillan, 472 pp.

Bogoliubov, N. N., and Y. A. Mitropolsky, 1961: *Asymptotic Methods in the Theory of Nonlinear Oscillations.* Gordon and Breach, 537 pp.

Charney, J. G., and J. G. DeVore, 1979: Multiple flow equilibria in the atmosphere and blocking. *J. Atmos. Sci.,* **36,** 1205–1216.

Collet, P., and J. P. Eckmann, 1980: *Iterated Maps on the Interval as Dynamical Systems.* Birkhäuser, 248 pp.

Curry, J. H., J. R. Herring, J. Loncarie and S. A. Orszag, 1984: Order and disorder in two- and three-dimensional Benard convection. *J. Fluid Mech.,* **147,** 1–38.

Davey, M. K., 1980: A quasi-linear theory for rotating flow over topography. Part 1: Steady β-plane channel. *J. Fluid Mech.,* **99**(2), 267–292.

——, 1981: A quasi-linear theory for rotating flow over topography. Part 2: Beta-plane annulus. *J. Fluid Mech.,* **103,** 297–320.

Denbo, D., and J. S. Allen, 1987: Large-scale response to atmospheric forcing of shelf currents and coastal sea level off the west coast of North America: May–July, 1981 and 1982. *J. Geophys. Res.,* **92,** 1757–1782.

Duffing, G., 1918: *Erzwungene Schwingungen bei veränderlicher Eigenfrequenz.* Braunschweig, 134 pp.

Enfield, D., and J. S. Allen, 1983: The generation and propagation of sea level variability along the pacific coast of Mexico. *J. Phys. Oceanogr.,* **13**(6), 1012–1033.

Feigenbaum, M. J., 1983: Universal behavior in nonlinear systems. *Physica,* **7D,** 16–39.

Guckenheimer, J., and P. Holmes, 1983: *Nonlinear Oscillations, Dynamical Systems, and Bifurcations of Vector Fields.* Springer, 453 pp.

Haidvogel, D., and K. Brink, 1986: Mean currents driven by topographic drag over the continental shelf and slope. *J. Phys. Oceanogr.,* **12,** 2159–2172.

Hale, J. K., 1969: *Ordinary Differential Equations.* Wiley and Sons, 332 pp.

Halliwell, G. R., Jr., and J. S. Allen, 1984: Large-scale sea level response to atmospheric forcing along the west coast of North America, summer 1973. *J. Phys. Oceanogr.,* **14,** 864–886.

Hart, J. E., 1979: Barotropic quasi-geostrophic flow over anisotropic mountains. *J. Atmos. Sci.,* **36,** 1736–1746.

Hirsch, M., and S. Smale, 1974: *Differential Equations, Dynamical Systems and Linear Algebra,* Academic Press, 358 pp.

Holmes, C., and P. Holmes, 1981: Second order averaging and bifurcations to subharmonics in Duffing's equation. *J. Sound Vibration,* **78**(2), 161–174.

Holmes, P., 1986: Chaotic motions in a weakly nonlinear model for surface waves. *J. Fluid Mech.,* **162,** 365–388.

Holmes, P. J., and J. E. Marsden, 1982: Horseshoes in perturbations of Hamiltonian systems with two degrees of freedom. *Commun. Math. Physics,* **82,** 523–544.

Kevorkian, J., and J. Cole, 1981: *Perturbation Methods in Applied Mathematics.* Springer, 558 pp.

Klein, P., and J. Pedlosky, 1986: A numerical study of baroclinic instability at large supercriticality. *J. Atmos. Sci.,* **43**(12), 1243–1262.

Lorenz, E. N., 1963: Deterministic nonperiodic flow. *J. Atmos. Sci.,* **20,** 130–141.

——, 1980: Attractor sets and quasi-geostrophic equilibrium. *J. Atmos. Sci.,* **37**(8), 1685–1699.

Martell, C. M., and J. S. Allen, 1979: The generation of continental shelf waves by alongshore variations in bottom topography. *J. Phys. Oceanogr.,* **9**(4), 696–711.

May, R., 1976: Simple mathematical models with very complicated dynamics. *Nature,* **261,** 459–467.

Melnikov, V. K., 1963: On the stability of the center for time-periodic perturbations. *Trans. Moscow Math. Soc.,* **12,** 1–56.

Miles, J., 1984a: Resonantly forced surface waves in a circular cylinder. *J. Fluid Mech.,* **149,** 15–31.

——, 1984b: Resonant motion of a spherical pendulum. *Physica,* **11D,** 309–323.

——, 1984c: Resonantly forced motion of two quadratically coupled oscillators. *Physica,* **13D,** 247–260.

Nayfeh, A., and D. Mook, 1979: *Nonlinear Oscillations.* Wiley and Sons, 704 pp.

Pedlosky, J., 1979: *Geophysical Fluid Dynamics.* Springer, 624 pp.

——, 1981: The effect of β on the chaotic behavior of unstable baroclinic waves. *J. Atmos. Sci.,* **38**(40), 717–731.

——, and C. Frenzen, 1980: Chaotic and periodic behavior of finite amplitude baroclinic waves. *J. Atmos. Sci.,* **37**(6), 1177–1196.

Peffley, M. B., and J. J. O'Brien, 1976: A three-dimensional simulation of coastal upwelling off Oregon. *J. Phys. Oceanogr.,* **6,** 164–180.

Perko, L. M., 1969: Higher order averaging and related methods for perturbed periodic and quasi-periodic systems. *SIAM J. Appl. Math.,* **17**(4), 698–724.

Preston, C., 1983: *Iterates of Maps on an Interval.* Springer, 204 pp.

Robinson, C., 1983: Sustained resonance for a nonlinear system with slowly varying coefficients. *SIAM J. Math. Anal.,* **14**(5), 847–860.

Rössler, O. E., 1976: *Physics Letters,* **57A,** 397.

Sanders, J., and F. Verhulst, 1985: *Averaging Methods in Nonlinear Dynamical Systems.* Springer, 247 pp.

Shaw, R., 1981: Strange attractors, chaotic behavior, and information flow. *Zeitschrift für Naturforschung,* **36a,** 80–112.

Shil'nikov, L. P., 1965: A case of the existence of a denumerable set of periodic motions. *Sov. Math. Dokl.,* **6,** 163–166.

Strub, P. T., J. S. Allen, A. Huyer, R. L. Smith and R. C. Beardsley, 1987: Seasonal cycles of currents, temperatures, winds and sea level over the northeast Pacific continental shelf: 35°N to 48°N. *J. Geophys. Res.,* **92,** 1507–1526.

Wolf, A., J. B. Swift, H. L. Swinney and J. A. Vastano, 1985: Determining Lyapunov exponents from a time series. *Physica,* **16D,** 285–317.